

# Airborne investigation of quasi-specular Ku-band radar scattering for satellite altimetry over snow-covered Arctic sea ice

Claude de Rijke-Thomas, Dr Jack Landy, Dr Robbie Mallett, Dr Rosemary Willatt, Dr Michel Tsamados and Dr Joshua King

**Abstract**—Surface-based Ku-band radar altimetry investigations indicate the radar signal is typically backscattered from well above the snow-sea ice interface. However, this would induce a bias in satellite altimeter sea ice thickness retrievals not reflected by buoy validation. Our study presents a mechanism to potentially explain this paradox: probabilistic quasi-specular radar scattering from the snow-ice interface. We introduce the theory for this mechanism before identifying it in airborne Ku-band radar observations collected over landfast first year Arctic sea ice near Eureka, Canada, in spring 2016. Based on SAR data, this study area likely represents level first year sea ice across the Arctic. Radar backscatter from the snow and ice interfaces were estimated by co-aligning laser scanner and radar observations with *in situ* measurements. On average, 4–5 times more radar power was scattered from the snow-ice than the air-snow interface over first-year ice. However, return power varied by up to 20 dB between consecutive radar echoes, particularly from the snow-ice interface, depending on local slope and roughness. Measured laser-radar snow depths were more accurate when radar returns were specular, but there was no systematic bias between airborne and *in situ* snow depths. The probability and strength of quasi-specular returns depend on the measuring height above and slope distribution of sea ice, so these findings have implications for satellite altimetry snow depth and freeboard estimates. This mechanism could explain the apparent differences in Ku-band radar penetration into snow on sea ice when observed from the range of a surface-, airborne- or satellite-based sensor.

**Index Terms**—Sea Ice, snow depths, Ku-band, Synthetic Aperture Radar (SAR), firstyear ice (FYI), multiyear ice (MYI).

## I. INTRODUCTION

**S**NOW depth estimates remain a large uncertainty for constraining the accuracy of sea ice thickness retrievals from polar altimetry (e.g. [1], [2], [3], [4], [5]). In the field of sea ice altimetry, there are numerous techniques that estimate sea ice thickness using Ku-band radar and some that estimate snow depth from the height difference between measurements from a laser and a radar altimeter. These tend to make the assumption that the Ku-band radar penetrates the full depth of the snow,

with the height of the maximum radar backscattering intensity equal to the height of the snow-ice interface [6], [1], [7], [8], based on the laboratory work of [9]. In contrast, neither an infrared nor green wavelength laser is assumed to penetrate into snow [10], [1]. However, surface-based measurements indicate between 1.5 and 5 times lower backscatter from the snow-ice interface compared to the air-snow interface [11], and the vertical distribution of backscattered power is highly variable depending on snow properties/conditions [12], [13]. For example, changes in snowpack properties such as temperature, salinity-induced liquid water, moisture content and density layering can reduce penetration of Ku-band radar and therefore raise the mean radar scattering surface [14], [12], [15], [16], [17]. In [18], for instance, the CryoSat-2 radar freeboard was found to vary over synoptic timescales as a function of new snowfall, air temperature and wind speed. Whilst the snow depth itself contributes to only around 10% of the sea ice thickness uncertainty, unaccounted for biases in the height of the principal radar backscattering intensity, caused by snow layer properties or snow brine volume for instance [16], [17] can contribute 24–32% of the ice thickness uncertainty [19]. The sea ice thickness uncertainty due to snow depth is a combination of snow impacts on the mean scattering surface of the radar as well as the availability of reliable snow depth estimates (e.g. [1], [20], [19], [5]).

There has been previous research into the impacts of snow roughness and snow properties on Ku-band radar penetration. During these studies, the relative impacts have appeared to depend on the scale of the observation. For example, *in situ* instruments such as the dual-frequency Ku/Ka-band radar, a surface-based and beam-limited radar system used on the MOSAiC expedition, have generally observed higher relative return powers from the air-snow interface than the snow-ice interface [13]. These results support previous observations from a sled-borne Ku-band radar over Antarctic sea ice, where the height of the mean radar backscattering intensity was located at only around 50% of the measured snow depth [12]. For airborne platforms, typically operating from an altitude between 0.5 and 10 km above the sea ice surface, it has been estimated that 80% of Ku-band radar returns originate closer to the snow-sea ice interface in snow temperatures  $\leq -8^\circ\text{C}$  [15]. However, over thicker snow covers or with warmer snow temperatures, airborne Ku-band SAR returns can be frequently retracked closer to the air-snow interface [15], [21]. King et al. [21] showed that airborne and CryoSat-2 satellite observations

Claude de Rijke-Thomas is with the School of Geographical Sciences, University of Bristol, UK (email: clauder@derijke.org). Jack Landy is with the Department of Physics and Technology, The Arctic University of Norway, Tromsø, Norway (email: jack.c.landy@uit.no). Robbie Mallett is with the Centre for Earth Observation Science, University of Manitoba, Canada, and also with the Centre for Polar Observation and Modelling, UCL, UK. Rosemary Willatt and Michel Tsamados are also with the Centre for Polar Observation and Modelling, UCL, UK. Joshua King was with the Climate Research Division, Environment and Climate Change Canada, Canada.

Manuscript received May 3, 2023; revised X X, 2023.

of sea ice freeboard over first-year ice with deep (40+ cm) snow at the N-ICE2015 site severely overestimated *in situ* measurements. However, there was a known thick bias present in the ESA Baseline-C freeboard observations used in this study [22].

The beamwidth of the Ku-band antenna of the surface-based KuKa radar is  $16.5^\circ$ , with a footprint size of  $0.4 \text{ m}^2$  [23], and the one-sided beamwidth of an airborne system is around  $1.2^\circ$  with a footprint of  $5 - 50 \text{ m}$  (e.g. [15]), which are geometrically very different to satellite footprints. For instance, the CryoSat-2 radar altimeter pulse-limited beamwidth is  $0.12^\circ$  and SAR-focused footprint is around  $380 \text{ m}$  along track  $\times$   $1650 \text{ m}$  across track [24] so the satellite encounters a very different range of incidence angles than the surface-based or airborne platforms. Here we use airborne Ku-band radar in combination with coinciding *in situ* observations to assess the impacts of snow, roughness and local slope on the backscattering properties of the sea ice surface. Using a geometry between *in situ* and satellite sensors helps to guide the interpretation of sea ice backscattering mechanisms between scales and challenge the assumption that satellite algorithms assume full penetration of the snowpack at Ku-band.

## II. NADIR KU-BAND RADAR SCATTERING THEORY OVER SEA ICE

Theoretical models generally predict that the Ku-band backscatter from snow-ice and air-snow interfaces is a combination of diffuse scattering and quasi-specular reflections, depending on the roughness and angle of incidence [25], [26]. The expected incoherent/diffuse proportion of radar backscatter consists of rough interface scattering [27] and volume backscatter from within the snowpack, from: internal interfaces or density transitions, snow grain shape, size and aggregation and snow depth and density (and hence snow-water-equivalence) [28], [12], [29], [30]. The quasi-specular component is predicted to be a combination of phase- and direction- coherent, direction-only-coherent (where the signal is scattered back in a uniform direction but out of phase) and incoherent/diffuse (random phase, random direction) [31]. The coherent backscatter from a slightly radar-rough surface at  $13.8 \text{ GHz}$ , characteristic of sea ice with rms height between  $0$  and  $0.7 \text{ cm}$  [32], can be expressed as [26], [33], [31]):

$$\sigma_{coh}^0 \approx 4|R_0(\theta)|^2 \frac{H}{c\tau} e^{-4(k^2\sigma^2 + \frac{\theta^2 H}{c\tau})} \quad (1)$$

where  $\sigma$  is the rms surface height,  $k$  is the wavenumber,  $R_0(\theta)$  is the Fresnel reflection coefficient,  $\tau$  is the pulse-width, and  $H$  is the height of the sensor above the surface. This accounts for the sphericity of the wavefront and assumes a Gaussian beam with a small pulse-limited beamwidth. The magnitude of the coherent component of the return is proportional to the distance of the target, such that  $\sigma_{coh}^0$  at zero incidence can vary by  $> 15 \text{ dB}$  for the range of altitudes between airborne and satellite platforms.

When a portion of the radar footprint contains sufficiently smooth ice to produce coherent returns, the quasi-specular backscattering component dominates [34], [35], [26], [33],

[36]. This is the case with smooth new sea ice growing in leads, where less than 1% of the footprint needs to contain this ice type before the coherent reflection dominates [33]. In this case the effective footprint of the altimeter echo can be as small as the first Fresnel zone, i.e. around  $180 \text{ m}$  in diameter [37]). However, it is still unclear from empirical studies over sea ice whether the diffuse or quasi-specular component generally dominates, whether they have similar magnitudes, or whether the relative contributions can vary with sea ice surface properties, snow cover, and importantly the geometry of the sensing platform.

The goals of this study are to investigate quasi-specular Ku-band radar altimeter returns observed over Arctic first-year sea ice from aircraft, and to present a plausible mechanism to explain them. A secondary objective is then to determine whether the Ku-band radar backscatter over sea ice is predominantly returning to the aircraft from the air-snow or snow-ice interface over first-year ice. By exploring the mechanism theoretically, a final objective of the study considers whether the same specular backscattering mechanisms are present in spaceborne Ku-band radar altimeter observations.

## III. DATASETS

For this work, NASA's Operation IceBridge Spring 2016 Ku-band SAR L1B Geolocated Radar Echo Strength profiles, Version 2 [38], were used, in combination with co-located Operation IceBridge L1B Airborne Topographic Mapper (ATM) measurements, Version 2 [39] to estimate snow depth and interface roughness (see below). The ATM is a scanning green-wavelength (532 nm) LiDAR developed by NASA, which we assume has negligible penetration into snow. The ATM laser has a spot diameter of around  $1 \text{ m}$  and a typical point spacing of  $2 \text{ m}$  with the conical scanning pattern providing higher point density at the edges of the swath [40], [41]. The airborne snow depth estimates were compared to coincident *in situ* magnaprobe snow depths from the Environment and Climate Change Canada (ECCC) 2016 Snow on Sea Ice Campaign near Eureka (described in [42]), which can be seen in Figure 1. A summary of the airborne instrument parameters can be seen in Table I.

Two sites of *in situ* measurements from the ECCC 2016 Snow on Sea Ice Campaign were examined: one landfast firstyear ice (FYI) site and one landfast multiyear ice (MYI) site. The FYI site can be seen in Figure 1. The FYI site central coordinate was  $79.9718^\circ \text{N}$ ,  $86.7912^\circ \text{W}$ , whilst the MYI site central coordinate was  $79.8137^\circ \text{N}$ ,  $86.8085^\circ \text{W}$ . The FYI site was described as 'moderately rough' FYI, compared to smoother ice found elsewhere in the area. Eight airborne flyovers took place over the FYI and seven over the MYI on the 19th April 2016, whereas the *in situ* measurements were taken on the 15th April for the FYI and 17th for the MYI sites. The FYI site was chosen for this study because there was  $< 1 \text{ cm}$  precipitation between the dates of *in situ* and airborne measurements (Government of Canada) [43]. The FYI *in situ* site spans just over  $1 \text{ km}$  by  $600 \text{ m}$ , whereas the

TABLE I

AIRBORNE INSTRUMENT PARAMETERS. NOTE THAT THE FOOTPRINT SIZE CHARACTERISES THE EXTENT TO WHICH THE RADAR ENERGY DECREASES TO A CERTAIN LEVEL DUE TO THE PULSE WIDTH OR SAR PROCESSING. STRONGLY BACKSCATTERING TARGETS FROM OUTSIDE THIS NOMINAL FOOTPRINT SIZE CAN STILL INFLUENCE THE RADAR RETURN, WITHIN THE ANTENNA BEAMWIDTH ( $\sim 45^\circ$  IN BOTH DIRECTIONS).

**CRISIS Ku-band radar altimeter**

Data description: FMCW along-track-SAR-processed  
(level 1B — deconvolved version)  
Effective pulse full-width at half-maximum: 0.3 ns  
Altimetric sample resolution: 1.30 cm in air  
Central frequency: 14.75 GHz  
Bandwidth: 5.78 GHz  
Footprint size: 4.5 m  $\times$  16 m at 500 m elevation  
Pulse-limited beam width:  $0.9^\circ$

**Operation IceBridge Airborne Topographic Mapper (ATM)**

Data description: canonically scanning lidar  
(level 1B — Version 2)  
Wavelength: 532 nm (green light)  
Altimetric uncertainty (measured here): 4.80 cm  
Spot resolution:  $\sim 1$  m  
Point spacing:  $\sim 2$  m

MYI *in situ* site spans just over 600 m by 400 m, including the ‘arms’ of snow measurements at each side (Figure 1). The average separation between *in situ* snow depth measurements was  $\sim 0.92$  m within the body of the FYI site and  $\sim 1.9$  m in the site ‘arms’, whereas for MYI the average separation was  $\sim 0.95$  m within the body of the site and  $\sim 1.45$  m within the site ‘arms’. 8092 magnaprobe snow depths were measured over FYI and 4073 over MYI. The measurements were conducted in evenly-spaced parallel lines across the sites. Measurements of temperature, salinity and density of the snow were also taken at 23 snow pits in the general area surrounding these sites. Three of these snow pits were taken within the FYI site in focus and two within the MYI site.

It is an important question how representative the sites were of ‘typical’ sea ice in the Arctic. Sea ice growing in a protected fjord environment, such as the area around Eureka, might be smoother than ice growing in the open Arctic Ocean. Therefore, we examined April 2016 observations from CryoSat-2, the Sentinel-1A C-band SAR, and the Multi-angle Imaging SpectroRadiometer (MISR), to place the Eureka sites into a wider context. The median CryoSat-2 waveform stack standard deviation and pulse peakiness were 10.9 and 0.045, respectively, for valid sea ice returns acquired within 100 km of the sites along a 16th April 2016 track. These values are representative of rougher FYI in the Arctic Ocean, with Zygmuntowska and Khvorostovsky (2014) [44] showing peaks at around 8 and 0.095 for pan-Arctic winter distributions of these two waveform parameters in regions of FYI. Sentinel-1 C-band backscatter from the Eureka FYI site is shown in the context of incidence angle-dependent backscatter curves from the pan-Arctic training database created by [45] in Appendix A3. Four April 2016 SAR images including the Eureka site confirm the C-band response was representative of ‘level’ FYI in the Arctic Ocean. Finally, the MISR sensor has been used to detect the air-snow interface roughness of sea ice during

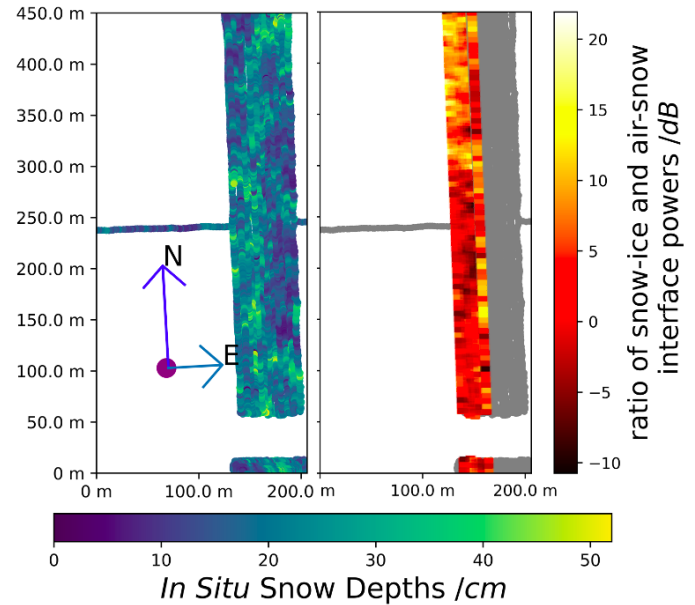


Fig. 1. Left: *in situ* magnaprobe snow depth measurements taken within the central part of the FYI site used in this study ( $79.9718^\circ\text{N}$ ,  $86.7912^\circ\text{W}$ ). Right: backscatter ratios between the snow-ice and air-snow interfaces for ku-band radar altimeter footprints corresponding to the FYI *in situ* site (underlaid in grey). The MYI site is not shown since the Ku-band SAR waveforms from it were too ambiguous to reliably make conclusions from in this study. The mean and standard deviation of *in situ* snow depths across the whole FYI site was  $20.4 \pm 8.0$  cm.

the Arctic spring [46]. MISR roughness observations from the Eureka FYI site in April 2016 were at almost exactly the modal pan-Arctic FYI roughness for the month (Appendix A2).

## IV. METHODOLOGY

### A. Instrument Calibration

Eight flyovers over the FYI site and seven over the MYI site were used in combination to increase the spot density of the ATM laser data and number of comparisons between radar and *in situ* data. By combining the flyovers, there was an average of 46 ATM laser points per Ku-band SAR footprint over FYI and 41 over MYI. The heights of the ATM laser data were referenced to the WGS84 ellipsoid. For the ATM altitudes in the flyovers to be comparable to each other, the ATM sample heights of each flight were aligned, to eliminate systematic uncertainty. This was done by making forty-nine 100 m diameter patches adjacent to and over the *in situ* sites, each containing laser data from each flyover, and calculating the mean of all the mean patch altitudes for each flyover, termed the ‘effective mean flyover altitude’. These averaged patches were used in order to remove bias due to variations in the sample density between flyovers. The means of the mean patch altitudes for each flyover can be seen in Appendix B4, and the  $\sim 10$  cm variations in height between flyovers shows that there are relatively small systematic uncertainties between tracks. These may be caused by changes in GPS accuracy or drift, the ATM sensor environment, or to background visible solar radiation depending on the time of day.

In order to do subsequent analysis, the random height uncertainty of the ATM laser points had to be assessed. This

was done by studying ATM samples over leads (the sea surface at cracks between diverging ice floes) across the Beaufort Sea on the following day, 20th April 2016. The random height uncertainty of the ATM laser was assumed to be similar over sea ice than measured over leads. Leads were classified from the pulse-peakiness of radar samples over the same locations as the ATM data. The pulse-peakiness of a waveform is defined by:

$$pulse\_peakiness = \frac{P_{max}}{\sum_{i=1}^n P_i} \quad (2)$$

where  $n$  is the number of range bins and  $P_{max}$  is the maximum linear power of the waveform.

Lead footprints were defined as having a pulse peakiness of at least 0.15, a maximum linear power return of at least 80, and also having a major peak width (the width of the highest peak in the waveform) corresponding to at most 5 range bins. The waveforms are uncalibrated, meaning the criteria assumes relative backscatter instead of absolute power. The criteria were verified by observing consistently level sets of consecutive samples in the Ku-band radar echograms, indicative of leads, as well as by visually identifying the same leads in IceBridge DMS L1B Geolocated and Orthorectified Images, Version 1 [47]. In addition to these criteria, a usable lead footprint had at least one footprint also identified as a lead within two footprints either side of it, ensuring that no sea ice samples at floe edges were used. To account for the smaller Fresnel-limited footprint of the radar return from leads (CReSIS 2017 [38]), the standard deviation of the ATM laser data was calculated at nadir from an area 1/3 the dimensions of the pulse-limited radar footprint. The random uncertainty of the ATM laser within leads was calculated to be 4.8 cm (but increased to 5.7 cm if the full footprint dimension was used).

The remaining analysis focuses on laser and radar data collected on the 19th April 2016 over the two landfast sea ice sites near Eureka. In many of the Ku-band radar waveforms, clear peaks (defined at the beginning of the next subsection) could be identified from both the air-snow and snow-ice interfaces, as shown in Figure 2. After the ATM and Ku-band radar data were aligned to the WGS84 ellipsoid, the approximate surface elevations from both sensors were within  $\sim 10$  cm from each other, but could not be assumed to be perfectly aligned. The ideal approach would be to align the two sensors absolutely at leads because at these locations there is a dominant return from the sea surface height for both instruments. However, there are typically few leads over landfast sea ice in the Canadian Arctic, including at Eureka in 2016. Therefore, a different method of aligning the Ku-band SAR altitudes to the ATM laser was applied. For footprints whose waveforms had clearly identifiable air-snow and snow-ice interface peaks (i.e., Figure 2(b)), the altitude of the radar return from the air-snow peak was compared to the mean ATM laser altitude of all points within the radar footprint. The relative height differences between the first peak in double-peaked echoes and their coinciding averaged ATM elevations were then averaged across each radar echogram in order for

the radar-derived interface elevations to be aligned to the ATM laser data.

## B. Retracking Interfaces and Snow Depth Estimation

To estimate the snow depth over sea ice, the retracked radar snow-ice interface peak was subtracted from the average ATM laser altitude, for all valid radar footprints. When analysing the Ku-band radar waveforms to estimate snow depths, the snow-ice interface needed to be clearly identifiable within the waveform. This meant that waveforms with merged peaks (having an unidentifiable drop to 50% power between peaks) or more than two prominent peaks (more than one above  $0.3 \times$  the maximum power before the primary peak or more than one within 80 cm after the first peak above  $0.4 \times$  the maximum power) could not be used, to ensure the 70% threshold assumed to represent the snow-ice interface could be accurately retrieved. Echoes with two prominent peaks were assumed to originate from the air-snow and snow-ice interfaces. Echoes with a singular major peak were assumed to originate from the snow-ice interface, because the snow-ice interface often appeared (91% of the time in FYI) to be more prominent in double-peaked echoes. If and when this assumption was invalidated, i.e. the single major peak originated from the air-snow interface, the derived snow depth would be underestimated.

A TMRA (Threshold Maximum Retracking Algorithm) with a 70% retracking amplitude was assumed to represent the height of interfaces in airborne radar returns. The choice of 70% is based on the theoretical retracking point for a SAR processed radar altimeter echo over a rough sea ice surface [48], [49], [50], [3]. (Note the same TMRA was applied to all clear peaks, up to a maximum of two, for the radar data in all echograms coinciding with the *in situ* sites.) The average differences in range between ATM laser data and the 70% thresholds of the air-snow interfaces for every flyover can be seen in Appendix B5. These offsets vary within the range of  $\sim 14$  cm, and there are similar offsets between the FYI and MYI sites, implying a slowly-varying time-dependent offset between the Ku-band radar and ATM laser instruments. Once all the offsetting had been applied, the estimated altitudes of the air-snow interface, using both ATM laser and Ku-band SAR, can be seen in Appendix B6. Note that this calibration technique was only possible due to the fine range resolution of 1.30 cm of the Ku-band radar altimeter.



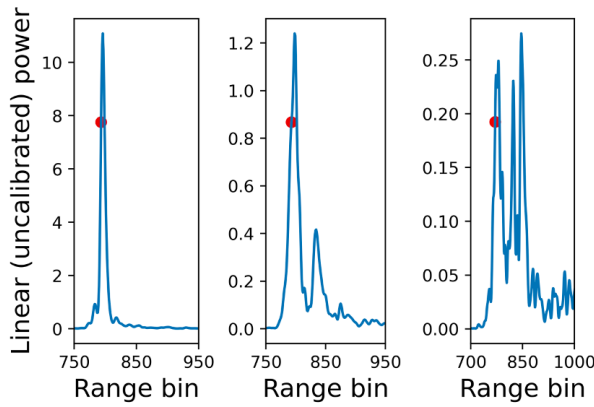


Fig. 2. Examples of characteristic waveforms. The red dots indicate the position on the leading edge of the waveform corresponding to 70% of the maximum power, and corresponds to the snow-ice interface peak in the first waveform, but the air-snow interface peak in the subsequent two waveforms.

Overall, 41% of the waveforms over FYI and 53% of waveforms over MYI were discarded when estimating snow depths. 13% of the FYI waveforms had more than two strong peaks, 18% had inseparable peaks, and 9% did not meet other filtering criteria given above. 24% of the MYI waveforms had more than two strong peaks, 13% had inseparable peaks, and 16% did not meet other filtering criteria. Note these waveforms were only omitted from the analysis of snow depths, but all usable waveforms were included in the analyses of power and energy returns from the snow-ice and air-snow interfaces (see below). These initial snow depths had to be corrected for the delayed radar wave propagation speed in snow, before they could be compared to the *in situ* magnaprobe snow depths. For this the refractive index was estimated from the mean density of the snow measured in FYI snow pits, being  $0.329 \text{ g cm}^{-3}$ , based on the equation of [35] and giving  $n = 1.262$ .

All sets of coincident radar, laser and *in situ* data, within a radar footprint, were used if the pitch and roll of the aircraft was  $< 3^\circ$ . The mean ATM laser elevation within a radar footprint, as well as the mean *in situ* snow depth within a footprint subtracted from the mean ATM laser elevation, were used as reference levels for the air-snow and snow-ice interfaces, respectively. The (uncalibrated) backscattered radar power from each interface was then estimated from the radar range bin located at these reference levels. This method assumes that the power at these points on the echo is primarily coming from the snow or ice located close to the nadir range to that point, without strong off-nadir contributions, as well as the Ku-band radar altitudes being appropriately aligned with the ATM laser altitudes (see appendix for further details), and so only serves as a close proxy to the relative backscattering of the air-snow and snow-ice interfaces. If the snow-ice interface peak originates from the farthest off-nadir point still within the footprint, the snow depth could be overestimated by a maximum of  $\sim 6 \text{ cm}$ . Additionally, if the retracking points are not situated on the interface peaks themselves, that would affect the estimated backscatter from the interfaces. Previous studies with the CReSIS S-to-C band ‘snow’ radar have shown that this first assumption is likely to be valid over undeformed

FYI but, over rougher MYI, returns from smooth hummocks outside the nadir point but within the beam-limited footprint of the altimeter can dominate the echo [51]. However, with the ku-band radar, there is no noticeable trailing edge bump in the airborne-estimated snow depth distribution when compared to the *in situ* observations, shown by Figure 4. The return powers of the two interfaces were also estimated by taking the powers of the two closest peaks to the reference levels, but the results were very similar.

### C. Footprint Roughness Estimation

To estimate the footprint-scale roughness of the air-snow interface, the standard deviation of the ATM laser elevations within a  $5 \text{ m}$  radius about the centre of the footprint was calculated. To estimate the footprint-scale roughness of the snow-ice interface, *in situ* snow depths were subtracted from ATM laser spots aligned within  $0.5 \text{ m}$  horizontally of each other. The footprint-scale roughness was estimated as the standard deviation of multiple snow-ice interface elevations within a footprint. At least 4 snow-ice interface altitudes were used with the mean number of points used  $7 \pm 4$ . Here we are limited by the spatial resolution of the aggregated ATM data (with the average distance to the nearest neighbouring ATM point within a footprint being  $0.85 \text{ m}$ ) which could be aliasing some of the true radar footprint-scale topography.

### D. Return Energy Estimation

To evaluate the relative contributions of radar backscatter from the snow-ice and air-snow interfaces to satellite waveforms, we can estimate the relative backscattered energy from the interfaces. This normalises the estimates of backscattered power from air-snow and snow-ice interfaces by the time taken for each increment of the radar pulse to propagate across the interface. One of the dielectric interfaces may produce a very strong return but the smooth footprint-scale topography of the interface could mean that the Ku-band pulse passes over the interface instantly. This would result in a strong but thin peak in the return power (of width equal to the transmit pulse width), occupying only a few range bins of the airborne radar which is several times finer than the range resolution of a satellite altimeter ( $\sim 40 \text{ cm}$ ). The influence of such a peak would be diluted at the satellite scale, appearing broader in a satellite waveform. Conversely, over an interface that spans over a large height range, there may be a moderate power return over a longer period of time, whilst the radar pulse passes over the interface, and this may influence the satellite waveform more. Thus, we can normalize by the time taken for each part of the pulse to cross the height variations (footprint-scale roughness) of an interface, in order to estimate the relative return energies from each interface, which is a better indicator of how the interface is likely to contribute to the return waveform of a satellite. (Note that this is not the normalised radar cross section because the backscattered power would need to be calibrated and the return normalised by the true footprint area.) The relative return energies should be independent of both the time taken for an increment of the radar pulse to travel over an interface within a footprint (due

to footprint-scale interface surface roughness) and altimetric range resolution.

The relative return energies of Ku-band radar backscatter from the air-snow and snow-ice interfaces have been estimated by multiplying the power of the return from the interface by the time it takes for the pulse to pass over the interface. The time the pulse takes to travel over an undulating interface, within the pulse-limited footprint, is taken to be proportional to the roughness of the interface, multiplied by the speed of propagation over the interface (using the refractive index of air for the air-snow interface, and the refractive index of snow for the snow-ice interface). The random uncertainty in the ATM elevation data had to be accounted for before they could be used for estimating the radar pulse travel time across the interfaces. The standard deviations of the interfaces within 5 m centered on each footprint were calculated as follows:

$$\begin{aligned} \text{interface\_standard\_deviation} = \\ \sqrt{(\text{measured\_standard\_deviation}^2 \\ - \text{ATM\_random\_uncertainty}^2)} \quad (3) \end{aligned}$$

where the ATM laser random uncertainty was  $\pm 0.048$  m. For all valid samples, the data were split into ten deciles based on snow depth and the mean interface standard deviations were multiplied by the mean power returns from the snow-ice and air-snow interfaces in each snow depth decile, to produce Figure 10.

#### E. Footprint Slope Estimation

For the estimation of across-track footprint slopes, all of the ATM laser data within the pulse-limited footprint ( $\sim 16$  m) was projected onto the across-track direction. Here we aim to examine the *relative* variations in radar return power, from each interface, as a function of the major slope, even though the  $\sim 16$  m scale may in reality be aliasing steeper facet slopes within the footprint. To ensure footprint-scale roughness co-varying with slope did not affect the results, only footprints with a standard deviation of the across-track-slope-compensated ATM laser data  $< 9$  cm were used. The slope was determined from a plane fit to all ATM samples within a footprint, projected onto the across-track direction.

### V. RESULTS

Measurements of temperature, density and salinity at the FYI and MYI snow pits were summarised, to assess the spatial variability of snow properties and their possible influence on Ku-band radar returns. These distributions through the snow pack can be seen in Figure 3. For the FYI site, the temperature profile varied on a smooth gradient from around  $-23^\circ\text{C}$  down to  $-17^\circ\text{C}$  at the base of the snowpack, due to the atmosphere being colder than the ocean, whilst the density profile decreased from around  $0.37 \text{ g cm}^{-3}$  to  $0.28 \text{ g cm}^{-3}$  going down through the snowpack. The top layer of the FYI snow comprised of small wind-rounded or faceted crystals that are well-bonded whereas the middle/bottom layers were loose prisms/cups and large-grained, indicative of lower density

depth hoar. There was almost no salt within the main body of the snow but the lower 20% of the snowpack had an average salinity of  $11 \pm 8 \text{ ppt}$ . For the MYI site, the mean salinity was  $< 1 \text{ ppt}$ .

During the ECCC 2016 Campaign, the air temperature was generally recorded as below  $-20^\circ$ . Across snow pits, the temperature gradient did not vary much. The density gradient for MYI was also generally consistent until near the bottom of the snow, with density variations due to either being less dense depth hoar or a very dense snow-ice slab layer at the bottom of the snow. For the FYI, there was a large variation in basal salinity, with the lower 20% ranging from  $0.1 \text{ ppt}$  to  $33 \text{ ppt}$ .

Over the FYI site, the mean and standard deviation of airborne-estimated snow depth was  $19.3 \pm 8.2 \text{ cm}$ , whereas the corresponding mean and standard deviation of *in situ* snow depth from the same radar footprints was  $21.1 \pm 5.2 \text{ cm}$ . The footprint-scale mean absolute difference between the airborne-estimated snow depths and *in situ*-estimated snow depths was calculated as  $4.82 \text{ cm}$ . A plot of footprint-scale, airborne-estimated snow depths compared to *in situ* measurements can be seen in Figure 4. These results show that over FYI, the laser-radar snow depths resolve the same major patterns as the *in situ* observations, with some differences. The distribution of airborne snow depths is wider than the distribution from *in situ* observations, with a few airborne samples showing up to  $15 \text{ cm}$  larger snow depths than the *in situ* data and others showing snow depths close to zero. The minimum snow depth measured *in situ* over FYI was  $1.39 \text{ cm}$ .

Over FYI the footprint-scale radar pulse-peakiness (PP) was found to strongly correlate with the mean absolute uncertainty in snow depth, as seen in Figure 5. This means that for peaky waveforms like Figure 2(a) where the location of the snow-ice interface is clear and there are no off-nadir reflections contributing to the waveform, the radar can accurately resolve the snow-ice interface. The absolute error in snow depth with respect to the *in situ* data is  $\sim 3 \text{ cm}$  for waveforms with  $\text{PP} > 0.06$  which integrates uncertainties from the radar and the ATM sensors. For broader radar waveforms more like Figure 2(c), with  $\text{PP} < 0.03$ , the absolute error rises to  $\sim 7 \text{ cm}$ .

At the MYI site, the mean and standard deviation of the airborne-estimated snow depth was  $30.9 \pm 34.5 \text{ cm}$  which was relatively close to the *in situ* mean footprint snow depth of  $31.1 \pm 14.4 \text{ cm}$ ; however, the footprint-scale mean absolute difference between them was  $21.7 \text{ cm}$ . The Ku-band radar waveforms over MYI were generally complex (Figure 2(c)), containing multiple peaks with a relative strength still accepted by our selection criteria (above) but were evidently often retracked incorrectly with the simple TMRA method. For peakier MYI waveforms, with a  $\text{PP} > 0.06$  (data not shown), the mean absolute snow depth error with respect to the *in situ* data was  $< 10 \text{ cm}$ , but for waveforms with a  $\text{PP} < 0.02$  the error was as high as  $40 \text{ cm}$ . The errors included 10s cm over- and under-estimates in snow depth compared to the *in situ* observations, reinforcing the challenge to correctly identify the snow-ice interface from a complex, multi-peaked Ku-band radar waveform over MYI. Since the laser-radar method could not accurately measure footprint-scale snow

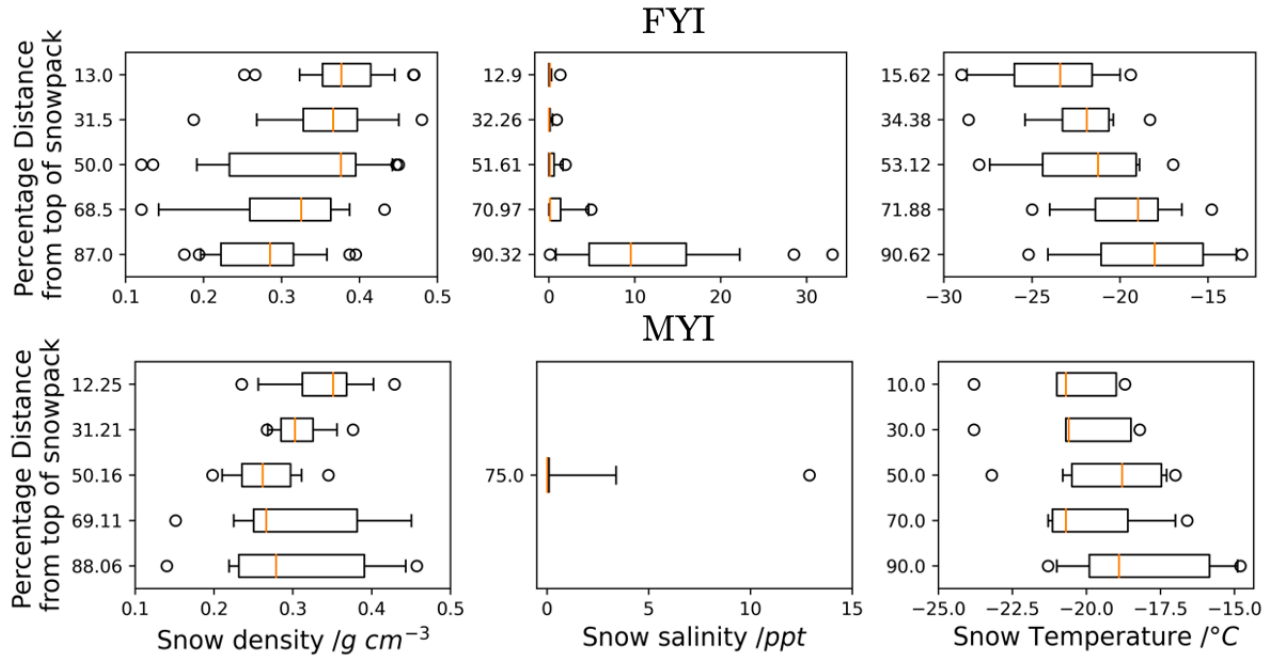


Fig. 3. Snow pit profiles of density, salinity and temperature around and within the first-year and multiyear sea ice sites (FYI and MYI) near Eureka. 23 were used in total, with 5 being MYI. The profiles are shown as a function of percentage depth through the snowpack, where 0% is the top of the snow and 100% is the bottom. The data is aggregated into pentiles. The orange lines represent the median values. The boxes encase the interquartile ranges and the whiskers show the 5th and 95th percentiles.

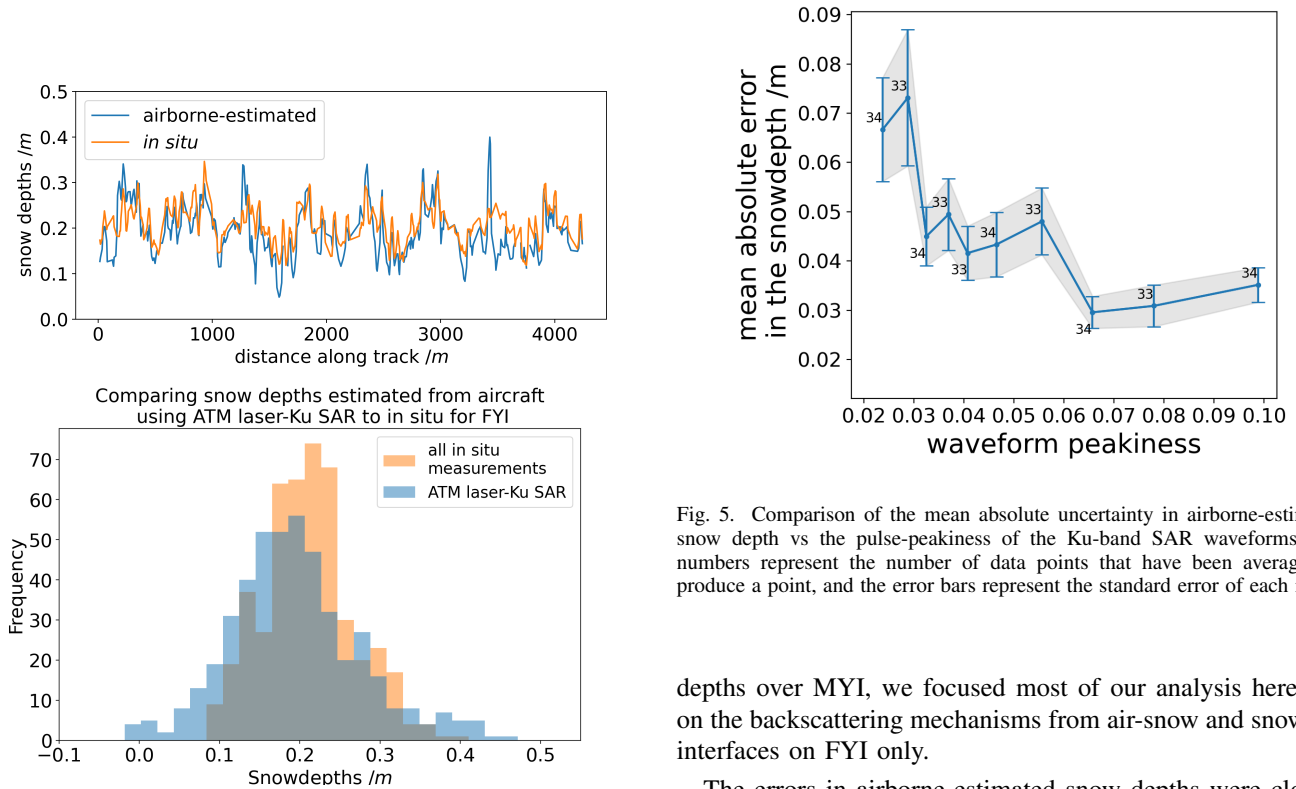


Fig. 4. Footprint-scale airborne-estimated snow depths compared to the mean *in situ* snow depths within the footprints. The moving average of the 4 closest footprints has been taken for both the airborne-estimated and *in situ* snow depths, for visual aid.

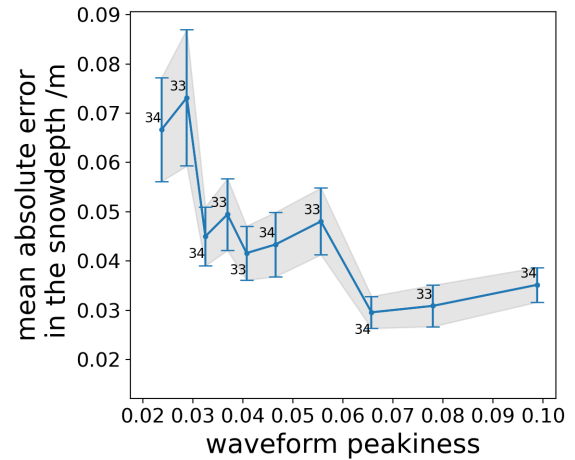


Fig. 5. Comparison of the mean absolute uncertainty in airborne-estimated snow depth vs the pulse-peakiness of the Ku-band SAR waveforms. The numbers represent the number of data points that have been averaged to produce a point, and the error bars represent the standard error of each mean.

depths over MYI, we focused most of our analysis hereafter on the backscattering mechanisms from air-snow and snow-ice interfaces on FYI only.

The errors in airborne-estimated snow depths were closely related to the surface roughness of the snow and sea ice. The mean absolute errors in snow depth increased as a direct function of the air-snow interface roughness derived from the standard deviation of ATM samples (Figure 6). For footprints with a roughness  $> 10$  cm, typical of the MYI site, the absolute errors were generally  $> 20$  cm supporting the results found

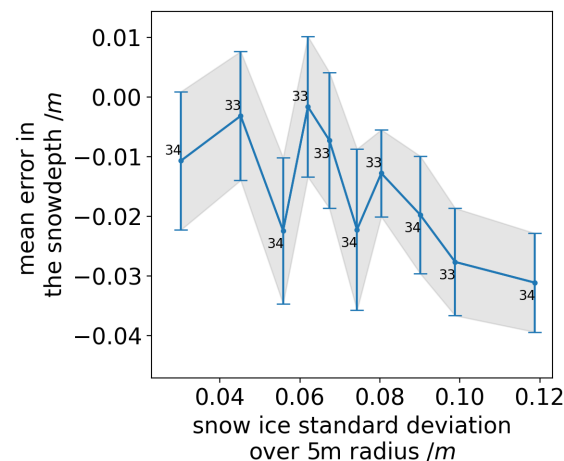


Fig. 7. Plot of mean error in airborne-estimated snow depth against standard deviations of the interfaces, over FYI. The error has been calculated by subtracting the *in situ* measurements from the airborne estimates. The numbers represent the number of data points that have been averaged to produce a point, and the error bars represent the standard error of each mean.

Figure 10 is a histogram showing the frequency distribution of linear (uncalibrated) power for two interfaces: Snow-Ice Interface (blue) and Air-Snow Interface (orange). The x-axis represents the linear (uncalibrated) power, ranging from 0 to 12. The y-axis represents the frequency, ranging from 0 to 175. The Air-Snow Interface shows a much higher frequency at low power values, peaking around 0.5, while the Snow-Ice Interface has a more uniform distribution across the range.

Authorized licensed use limited to: University College London. Downloaded on October 03, 2023 at 14:37:20 UTC from IEEE Xplore. Restrictions apply.  
© 2023 IEEE. Personal use is permitted, but republication/redistribution requires IEEE permission. See <https://www.ieee.org/publications/rights/index.html> for more information.

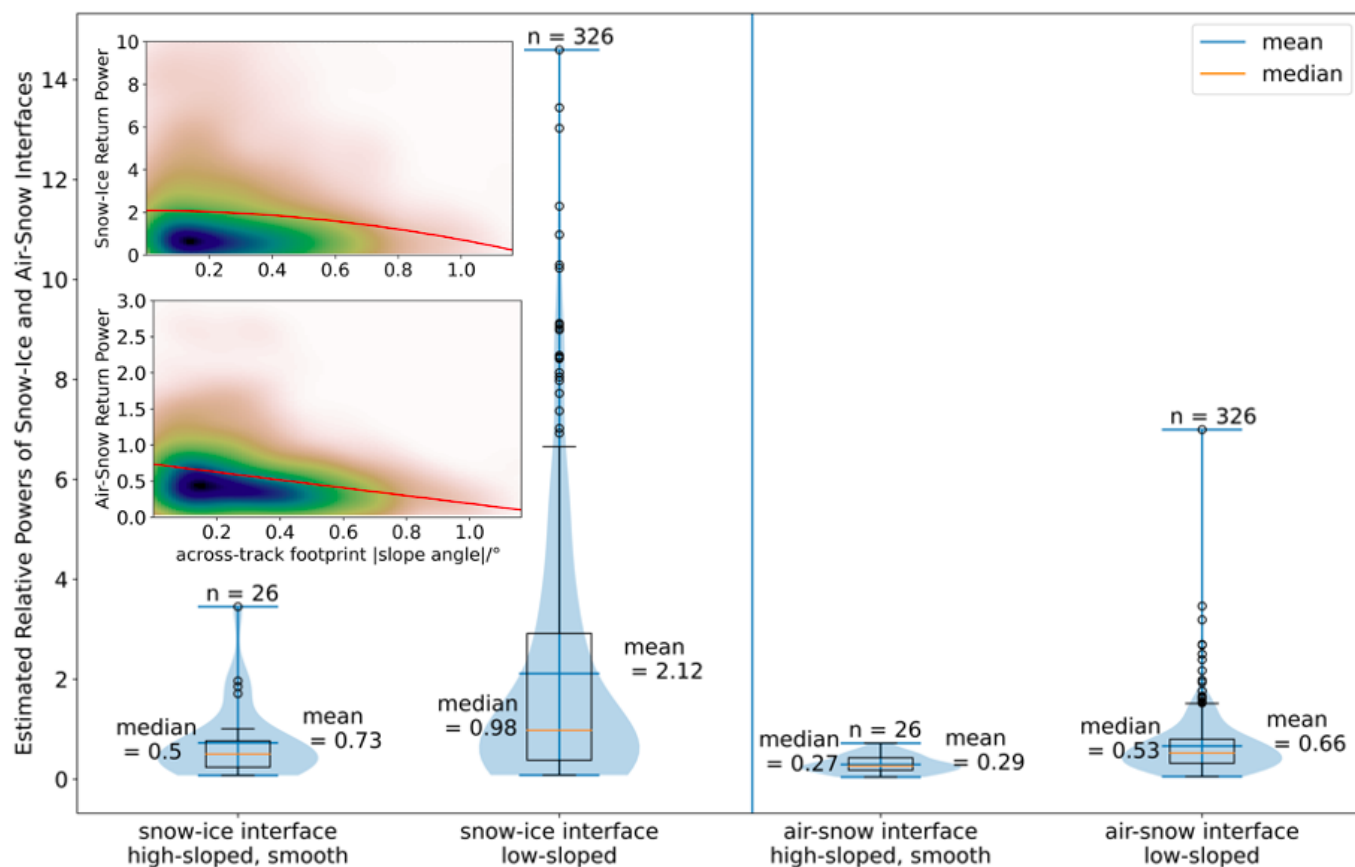


Fig. 9. A comparison between the power returns of the snow-ice (left) and air-snow (right) interfaces for first-year sea ice, comparing level ( $< 0.2^\circ$ ) footprints with smooth, sloped footprints ( $> 0.8^\circ$ , with values no higher than  $1.3^\circ$ ). Inline left: probability distribution functions of the linear return powers from the snow-ice (top) and air-snow (bottom) interfaces, against footprint slope angle, using a Gaussian kernel-density estimate. The fitted equation for the snow-ice interface is  $y = 1887.2 - 1885.1e^{0.000724x^2}$ , and for the air-snow interface is  $y = 0.734 - 0.544x$ .

snow-ice interface were also calculated for the maxima of the peaks nearest to the 70% retracking points for the interfaces. When this second method was used, the same patterns could be seen and the mean ratio of maximum powers between the snow-ice and air-snow interface peaks was 4.6, similar to the original 4.8. Subsequent return energy estimates would also not be insensitive to threshold choice, since these are proportional to the return powers. Based on these checks, defining individual retracking thresholds for the air-snow and snow-ice interfaces that varied with the roughnesses of the interfaces seemed unnecessary. The snow-ice interface return power distribution over FYI has a skew of 4.92, compared to 3.66 for the air-snow interface. These differences in the shape and statistics of the distributions have implications for the type of Ku-band radar scattering mechanism operating at the two interfaces.

To evaluate the physical reasons behind these strongly positively skewed distributions of relative powers, and their differences, the relative interface powers were assessed as a function of the local slope angle and interface roughness. The local slope angle of the sea ice surface was assessed over a scale of  $\sim 16$  m in the across-track direction within the radar footprint, estimated using all ATM points within a footprint projected onto the across-track direction. A comparison was made between footprints with relatively higher slope ( $> 0.8^\circ$ ,

but no larger than the maximum measured slope of  $1.3^\circ$ ) and lower ( $< 0.2^\circ$ ) across-track slope angles, as seen in Figure 9. There is a strong difference between the backscattered powers from the interfaces over level sea ice versus sea ice with a modest slope, relative to the aircraft antenna boresight. For the air-snow interface, the return power approximately doubled over level compared to modestly sloped surfaces, whereas for the snow-ice interface, the return power trebled over level compared to the sloped surfaces.

On average, the power backscattered from the snow-ice interface over FYI is several times higher than the power backscattered from the air-snow interface. However, from an airborne platform the Ku-band radar backscatter can still regularly be higher from the air-snow than the snow-ice interface, at a single footprint. Furthermore, the backscattered power tails off rapidly as the incidence angle from the radar to the surface increases, and the rate of reduction in power appears to be faster for the snow-ice than the air-snow interface, as seen in Figure 9. These findings suggest that Ku-band radar scattering mechanisms from snow and ice surfaces have a strong non-linearity, which we will visualise and discuss below.

The estimated return energies from the air-snow and snow-ice interfaces can be seen in Figure 10. The energy backscattered from the air-snow interface around nadir is estimated to be significantly lower than the energy backscattered from the



snow-ice interface around nadir. The return energy decreases for the air-snow interface as snow depth increases, which we would not expect if the results were totally independent of surface roughness. Although the impacts of travel time across the rough interface have been accounted for, there is still evidence for the correlation between rougher sea ice and thicker snow depth affecting the backscattering coefficient of the air-snow interface. Based on these results, it is expected that a Ku-band satellite altimeter return is more likely to sense the snow-ice interface than the air-snow interface, over first-year sea ice with similar ice and snow properties to the field site at Eureka. However, the relative differences in return energy are not so extreme that we can always assume this to be the case.

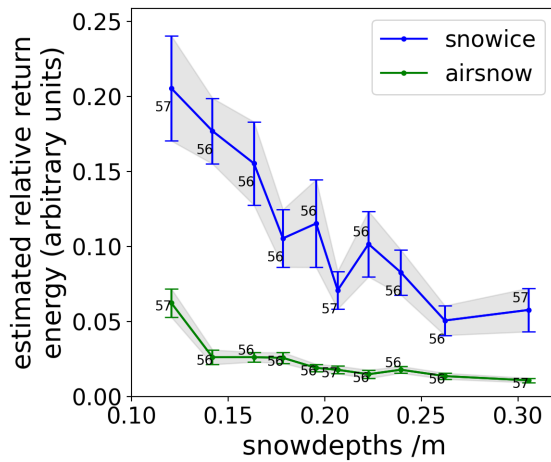


Fig. 10. Estimated relative return energies for both the air-snow and snow-ice interfaces, for different snow depths, over firstyear ice.

## VI. DISCUSSION

Past studies have suggested that snow layering, grain size, density transitions, and snow volume salinity-induced liquid water, as well as sea ice surface roughness, can impact the height of the principal Ku-band radar scattering horizon over sea ice [14], [12], [15], [52], [16], [17], [19]. Biases in the height of the principal backscattering intensity have a direct impact on the accuracy of sea ice freeboard and thickness estimates, and snow depth estimates from combined satellite laser and radar altimetry, which assume that the snow-ice interface dominates the radar backscattering intensity. Here we have been able to evaluate the impacts of snow volume salinity and density, snow and sea ice surface roughness at circa meters scale, and local slope, on the principal scattering depth of airborne Ku-band radar into snow-covered sea ice. We could not reliably assess the impacts of snow layering, grain size or snow density transitions. Although satellite altimeter footprints are sufficiently large for the sea ice to be assumed level with respect to nadir, we have used the across-track slope of airborne radar footprints over  $\sim 16$  m scale to examine the backscattering signature of the Ku-band radar over sea ice as a function of the incidence angle.

### A. Snow Volume Impacts

Radar modelling based on field observations of snow volume salinity in the Canadian Arctic has suggested that salt in snow can strongly attenuate Ku-band radar wave propagation by increasing the dielectric constant of snow grain scatterers. Modelling results indicate this process can raise the height of the maximum radar backscattering intensity by up to 7 cm over FYI [17], [53]. Salt was observed at the snow pits on FYI in our study, with snow salinities of 1.3 ppt measured in the uppermost 3 cm of snow at one pit. Generally, the depth hoar layers present at all 18 snow pits on FYI contained high salt contents with an average salinity of 5.0 ppt measured at the base 3 cm of the snowpack, and an average of 17.5 ppt at the snow-ice interface.

In spite of these measured salinities, there was no clear evidence that liquid water from snow volume salinity critically limited the penetration of airborne Ku-band radar into snow on FYI. There was a very small but significant ( $t$ -test = 4.1, two-tailed  $P$ -value equals 0.00004) difference between the per-footprint mean laser-radar snow depth of 19.3 cm and the *in situ* snow depth of 21.1 cm. This 1.8 cm difference may be attributable to retracking the snow-ice interface slightly upslope in sloped footprints, electromagnetic bias (described later), wave attenuation due to salt presence or a combination of these factors. The relatively high standard deviation of the laser-radar snow depth distribution (8.2 cm versus 5.6 cm for the *in situ* data) can be partially explained by the 4.80 cm random height uncertainty of the ATM sensor.

### B. Air-Snow and Snow-Ice Interface Scattering

Many of the results presented here give strong evidence for probabilistic quasi-specular scattering of the Ku-band radar from air-snow and particularly snow-ice interfaces over sea ice. Comparing the relative return power between radar footprints with different across-track slopes, there was a significantly stronger return from the low-sloped footprints, i.e. those orthogonal to the radar antenna boresight direction. Eq. (1) indicates that a coherent reflection from a relatively smooth sea ice surface facet should be highly nonlinear as a function of the incidence angle. A facet can be defined as a tilted but near-flat ‘radar rough’ patch with horizontal dimensions between the resolution of the aggregated ATM data ( $\sim 0.25$  m) and the radar-scale roughness ( $\sim 0.01$  m). If facets of the air-snow and snow-ice interfaces act as quasi-specular scatterers at Ku-band, we should therefore expect a disproportionate impact of these facets on the overall radar return. Based on Eq. (1), the disproportionately strong returns within the tail of the snow-ice power distribution in Figure 8 should occur when the snow-ice interface facets probabilistically align with the antenna boresight direction (or the nadir direction for a satellite platform). The fact this occurs more frequently for the snow-ice than the air-snow interface could be due to more sea ice facets facing orthogonal to nadir, the dielectric contrast being higher across the snow-ice interface, and/or to the snow-ice interface having a smaller radar wavelength-scale roughness than the air-snow interface. All three factors affect the coherent backscatter described by Eq. (1).



Further evidence for this probabilistic quasi-specular scattering of the snow-ice interface comes from the power of the backscattered radar return being around five times stronger, on average, from the snow-ice interface than from the air-snow interface. This is despite the air-snow interface providing a stronger return for around 30% of the individual radar returns. This is reinforced by the abrupt increase in return power from the snow-ice interface compared to the air-snow interface seen in a small proportion of waveforms in Figure 8. The error in laser-radar snow depth with respect to the *in situ* data decreases as a function of the radar waveform peakiness and increases as a function of the surface roughness. A peakier radar waveform represents a stronger and likely more coherent return, suggesting that the snow-ice interface elevation is retracked more accurately (i.e. snow depth is retrieved with lower error) when the radar echo is dominated by strong snow-ice interface reflection. Moreover, the rougher either interface becomes, the less likely the radar return is dominated by specular scattering and the error in retrieved snow depth increases (Figure 5). This provides empirical evidence for the scattering mechanism described by Eq. (1), and potentially helps explain the findings of [18]. The radar freeboard could vary over synoptic timescales, as the roughness/prominence of the air-snow interface changes in response to new snowfall or wind redistribution [18]. The relative energy returning from the snow-ice interface is generally significantly higher than the air-snow interface, and the ratio decreases with increasing snow depth, which is likely due to attenuation of the radar signal as it travels through the snow (Figure 10). [18] observed that snow accumulation can drive short-term increases in the measured radar freeboard, however this behaviour is suppressed in areas of the Arctic Ocean traditionally covered by multiyear ice. Our analysis may partially explain this phenomenon, with highly-specular returns expected from the surfaces produced by refrozen melt ponds. We note that melt ponds do not have to be exposed to or visible from the air to form these highly level surfaces, with subnivean formation also being a possibility [54]. While multiyear ice is in general rougher (e.g. [55]), it is possible that a relatively small coverage of highly level ponds would contribute to a disproportionately strong radar response from the snow-ice interface due to coherent effects. This could account for the higher-resistance of multiyear ice to the radar-freeboard response to snow accumulation documented by [18].

### C. Translating Airborne to Satellite Scales

It would be most valuable to know how these findings at the airborne scale (altitudes  $\sim 0.5$  km, footprints  $\sim 15$  m) translate to much larger satellite scales (altitudes  $\sim 700$  km, footprints  $\sim 1500$  m), to support the interpretation of satellite radar altimeter observations over sea ice and the assumptions taken in their processing. However, this is a significant challenge with empirical observations only collected at discrete scales (i.e. surface-based, airborne, and satellite), rather than evenly across the spectrum of scales.

Firstly, it is unclear whether a specular return from sea ice on the satellite scale would be predominantly phase-coherent or just direction-coherent. However, for the

interpretation of satellite altimetry returns from sea ice there is commonly an assumption that snow and ice scatterers sum non-coherently [56]. A Cryosat-2 SARIn track from 4th November 2012 (start time 13:34:15 UTC) was therefore used to examine the radar interferometer phase and coherence of waveforms backscattered from different sea ice types in the Canadian Arctic Archipelago (CAA) and ‘Wingham Box’ of the Central Arctic. The Canadian Ice Service chart for 5th November 2012 shows predominantly newly-forming grey-white ice for along-track observations in the CAA and multi-year ice for observations in the Wingham Box ([https://ice-glaces.ec.gc.ca/www\\_archive/AOI\\_10/Charts/sc\\_a10\\_20121105\\_WIS56SD.gif](https://ice-glaces.ec.gc.ca/www_archive/AOI_10/Charts/sc_a10_20121105_WIS56SD.gif)). The phase coherence at the waveform leading edge should mainly represent the coherence of the surface backscattered/reflected response reaching the twin CryoSat-2 antennae. This was estimated by calculating the mean coherence between 5 and 100% of the waveform leading-edge power for every sea ice waveform in the track. Figure 11 demonstrates that the leading-edge coherence is almost always  $> 0.9$  for this track and varies as a clear function of the full-waveform pulse peakiness and backscatter coefficient. Using SKLearn K-Means clustering on the  $\sigma^0$  and PP data [57], the mean leading-edge phase coherences of FYI, MYI and leads could be found. The cluster of phase coherence with a mean of 0.969 represents observations from newly-forming FYI in the CAA whereas the cluster with a mean of 0.938 represents MYI in the Wingham Box. The observations with phase coherence close to 1 (mean = 0.987) and high peakiness represent leads. These results suggest there is strong phase coherence in the initial backscattering response, at the waveform leading edge, for all sea ice surfaces. However, the coherence of the response increases for younger, smoother sea ice surfaces, indicating that the phase-coherent part of the specular reflection gets stronger with a smoother surface (i.e. a distribution of surface facet slopes closer to zero).

A theoretical approach can then be taken to try to bridge the airborne and satellite scales. The ratio of energy backscattered from the snow-ice interface to the air-snow interface depends, among other factors such as the dielectric contrast across the interfaces, on the coherent contribution to the observed specular reflections. Based on our airborne results, the quasi-specular scattering mechanism appears to start contributing to the backscattering of the Ku-band radar around nadir from somewhere between surface-based and airborne scales and beyond. Strong evidence for quasi-specular scattering has not been observed with surface-based Ku-band radar systems [13], [11]. Since the coherent contribution is proportional to the height above the sea ice (Eq. (1)), it might be expected that the ratio of coherent to incoherent backscattering power increases from airborne to satellite altitudes. For the most level surfaces, like leads, the effective area of the satellite footprint contributing to the radar echo is also likely to be reduced to the scale of the first Fresnel zone ( $\sim 180$  m). The effective footprint of the satellite altimeter will be inversely proportional to the ratio of coherent to noncoherent backscattering power [58]. Airborne observations presented here suggest that quasi-specular reflection is more likely from the snow-ice than

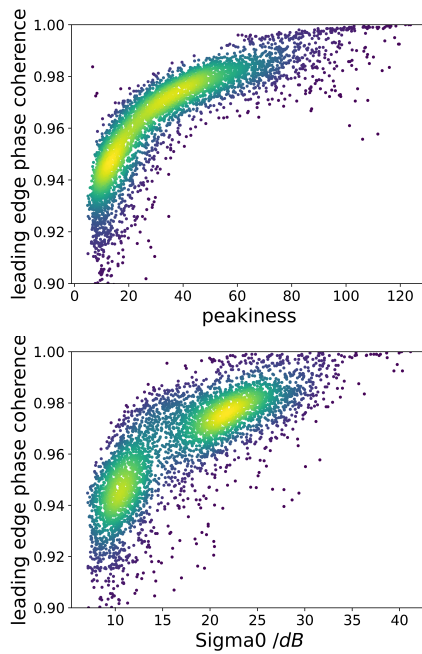


Fig. 11. Top: leading edge coherences of return waveforms against pulse-peakiness of a Cryosat-2 SARIn track that contains both FYI and MYI. Bottom: leading edge coherences of return waveforms against backscatter for the same track.

the air-snow interface. An increase in the ratio of coherent to non-coherent scattering at satellite scales should therefore increase the probability of the snow-ice interface dominating the waveform return.

The coherent contribution to the backscattering signature of sea ice at Ku-band is shown in Figure 12 for a radar incident to the snow-ice interface. Note that this does not include attenuation or Rayleigh scattering through the snow, and is just imagining a purely in-phase radar incident to the snow-ice interface. For reference the expected coherent backscatter for a satellite altimeter such as CryoSat-2 is also shown. To plot this figure, the Fresnel reflection coefficient of the snow-ice interface is assumed to be a constant 0.33, using the real parts of the relative dielectric constants of ice and snow calculated to be 3.17 and 1.59 respectively using [59]. The coherent backscattering coefficient depends closely on the radar wavelength-scale ( $0.5\text{ mm} - 5\text{ mm}$ ) surface roughness, which is challenging to measure over sea ice and therefore represents a major source of uncertainty on these calculations. (Note that the estimates of roughness we present here from the airborne ATM sensor represent larger horizontal scales of the sea ice roughness on the order of  $\sim 10 - 100\text{ cm}$ , more representative of the distribution of surface facet slopes). So, in Figure 12 the upper and lower bounds of the coherent backscattering coefficient are shown for a wide expected range of surface roughness heights:  $0.5$  to  $5.0\text{ mm}$ . This is based on field measurements collected over many artificial and natural types of snow and sea ice [60] [61] [62].

The observed power returns relative to across-track slope angle (i.e., the backscatter signatures), from the inset panels of Figure 9, are re-plotted in Figure 13. We show, alongside this,

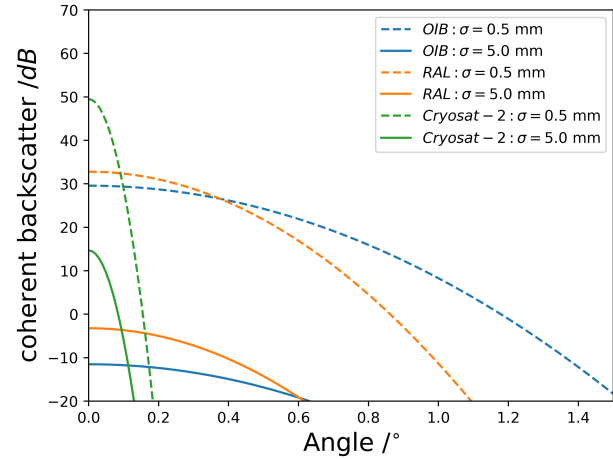


Fig. 12. Coherent backscatter for pulse-limited Ku-band radar incident to the snow-ice interface, at  $14.75\text{ GHz}$ ,  $515\text{ m}$  elevation and a pulse width of  $0.427\text{ ns}$ , representing the OIB Spring 2016 campaign, as well as a pulse-limited  $13.575\text{ GHz}$  Ku-band radar at  $730\text{ km}$  elevation with a pulse width of  $3.125\text{ ns}$ , representing CryoSat-2. The reflection coefficient is taken to be 0.25, representing a snow-ice transition [63].

the theoretical coherent return as a function of slope from Eq. (1). We also show the change in power as a function of slope modelled by the Updated Integral Equation Model (I2EM), which assumes backscattering from a single-roughness-scale random surface [27], [64], [65]. This model assumes non-phase coherent returns, as the community still conventionally does on the satellite scale [56]. We finally show the functional fit of a Lambertian return, representing perfectly diffuse scattering. The theoretical functions are referenced to the same relative return power at zero across-track footprint slope observed from the snow-ice interface. It is clear that the shape of the observed snow-ice backscatter signature lies somewhere between the theoretical predictions of the coherent and I2EM models. The reduction in snow-ice interface backscattered power with footprint slope (roughly fourfold over a degree change in slope) is too rapid to be described only by an incoherent scattering mechanism. However, it falls off too slowly to be described only by perfectly coherent reflection.

Figure 12 illustrates the expected coherent response with incidence angle for a level surface; however, sea ice is rarely perfectly level and we have observed the critical impact of local slope (Figure 9). Therefore, we estimate distributions of facet slopes from the ATM observations at our FYI and MYI sites at Eureka, as shown in Figure D8, through the method described in the appendix. The expected coherent radar response is then estimated from the average coherent backscatter shown in Figure 12, for a range of radar-scale roughness  $\sigma$  values, integrated over the observed distributions of facet slopes. The same approach is taken to estimate the expected non-coherent response from the backscatter coefficient predicted by the I2EM integrated over the same observed distributions of facet slopes. The correlation length  $l$  of the small-scale roughness is also required for I2EM and, since this parameter is also uncertain we recalculate the non-coherent

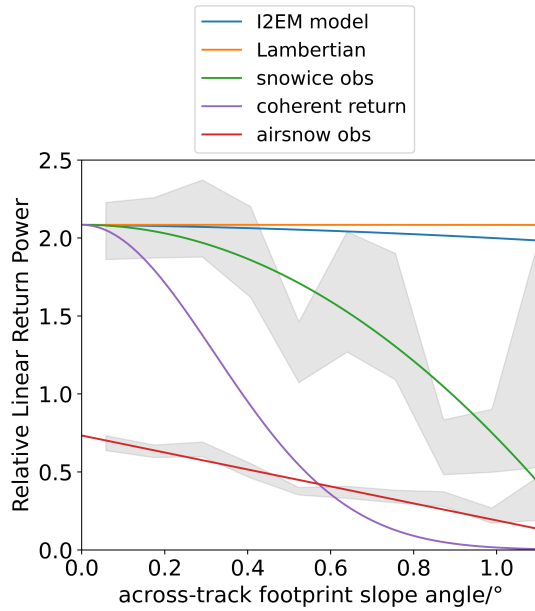


Fig. 13. A comparison between both observed and modelled linear power returns of the snow-ice interface and footprint across-track footprint slope angle. The I2EM model shown here has been tuned with mean values of 0.22 *cm* for the rms height and 1.24 for the correlation length as observed over sea ice in [62]. The functional fit of a Lambertian return is also shown, representing perfectly diffuse scattering. The fitted equation for the snow-ice interface observations (in green) is  $y = 1887.2 - 1885.1e^{0.000724x^2}$ , and for the air-snow interface (in red) is  $y = 0.734 - 0.544x$ .

response from I2EM for a wide range of values for  $l$  as well as  $\sigma$  based on field measurements [60] [61] [62]. This analysis produces theoretical estimates for the coherent and noncoherent backscatter recorded by a satellite for the same sea ice surface topography. The ratio of coherent to noncoherent backscatter is shown in Figure 14 with lines indicating the roughness bounds and points indicating realistic central values for  $\sigma$  and  $l$  of 0.0022 *m* and 0.0124 *m*, respectively.

For the CReSIS Ku-band radar, for a perfectly level ice surface with a radar-scale rms roughness of 1 *mm*, the ratio of coherence:incoherence at nadir is  $\sim 2,500$  (34 dB). Even for a level surface with significant small-scale roughness (3.1 *mm*), the ratio at nadir is  $\sim 63$  (18 dB). This suggests that at the altitude of the aircraft, a significant coherent response should be observed over sea ice if sufficient sea ice facets (with scale  $\sim 0.01$  to 1 *m*) face the antenna boresight direction. Given the ratio between the backscattered power from the snow-ice to the air-snow interface was only around five, there is likely to be a quasi-specular scattering mechanism from the air-snow interface too, not just the snow-ice interface (i.e. the air-snow interface is not a purely incoherent scatterer). This cannot be explained by lower coherent scattering from the snow-ice interface because the backscatter distributions from both interfaces were highly skewed (Figure 8). When the coherent response is integrated over the distribution of facet slopes for FYI, the ratio of coherent:incoherent backscatter reduces to  $\sim 8.6$  (9.3 dB) (Figure 14). This is very similar to

the difference between the upper and lower quartiles of relative backscattered powers from the snow-ice interface (Figure 8) which represent a ratio of around 15. The airborne Ku-band backscattering from the snow-ice interface does not fall off with incidence angle as quickly as the coherent model in Eq. (1) predicts (Figure 13). This is expected if only a fraction of the radar footprints investigated here, rather than all of them, had sea ice facets facing near-directly the radar antenna boresight.

Transitioning from OIB to a satellite altimeter such as Cryosat-2, the predicted ratio of coherent:incoherent (I2EM) backscatter actually decreases from 8.6 (9.3 dB) to 3.5 (5.4 dB), using the estimated facet slope distribution of FYI from our Eureka study site. Based on this facet slope distribution, the ratio reduces at satellite scales because the drop-off in backscatter with angle is steeper than for airborne scales (Figure 12), mitigating the fact that coherent backscatter from a flat surface increases linearly with range (see Eq. (1)). This means that, at satellite scales, fewer of the sea ice facets may face the radar to produce a strong coherent response. The ratio decreases from 4.67 (6.7 dB) to 0.70 (-1.6 dB) from OIB to Cryosat-2, using the estimated angular distribution over MYI, because the distribution of facet slopes is larger over MYI. Over smoother ice, with a shallower distribution of facet slopes, we would expect an increase in these ratios. The caveat to Figure 14 and to this discussion is that the distribution of facet slopes strongly depends on the resolution at which slope is sampled, and we are limited here to the resolution of the ATM data ( $\sim 1$  *m*). A finer sampling resolution could in theory result in a wider distribution with more low- and high-angle facet slopes, but it depends on the sea ice roughness properties at scales below the aggregated ATM point density. Furthermore, we use slopes calculated from the air-snow interface (i.e., ATM data) which (Appendix A2) suggests was rougher than the snow-ice interface (Appendix A3) for Eureka in April 2016. The ratio of coherent:incoherent backscatter increases as the distribution of facet slopes gets shallower, so if the snow-ice interface topography was smoother than the air-snow at Eureka, then using the ATM slope distribution would underestimate the expected coherent contribution. Conversely, if the snow-ice interface topography is generally rougher in the Arctic Ocean than the ATM topography measured at Eureka, then the expected coherent contribution would be smaller.

Observations of the sea ice-covered ocean in the Central Arctic in winter from CryoSat-2 show backscattering coefficients ranging from 10 to 40 dB [66] representing a ratio in power of 1000. Although the highest backscattering coefficients are produced by coherent reflections of the radar from new level ice in leads, there is a large transition zone from  $\sim 15 - 25$  dB where significant numbers of peaky CryoSat-2 waveforms do not come from leads or mixed lead-ice combinations [67]. Based on the theory of [26] and [31], and our observations from airborne Ku-band radar, variations in the coherent backscattering contribution from level ice around nadir could be primarily responsible for the  $10-100\times$  ratio of backscattered power between pure diffusely scattering ice floes and highly specular scattering floes in CryoSat-2 data. This ratio is towards the upper bound of our

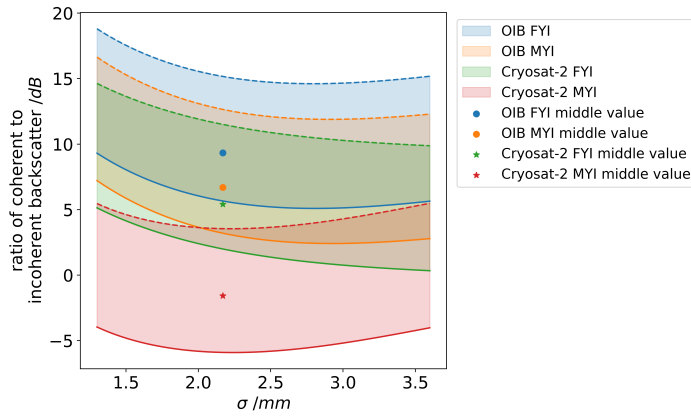


Fig. 14. Ratio of coherent to I2EM backscatter for pulse-limited Ku-band radar at 14.75 GHz, 515 m elevation and a pulse width of 0.427 ns, representing the OIB Spring 2016 campaign, as well as a pulse-limited 13.575 GHz Ku-band radar at 730 km elevation with a pulse width of 3.125 ns, representing CryoSat-2. The spread of the values for each class is determined by the  $\pm 1$  standard deviations of the correlation lengths ( $l = 0.62$  cm and  $l = 1.86$  cm, represented by the solid and dashed lines respectively) found in [62], over a diverse range of ice types. The mean observed  $\sigma$  and  $l$  values in [62] are shown by the dots. The ratio of coherent to I2EM backscatter is independent of the reflection coefficient.

approximate theoretical predictions in Figure 14, based on the facet slope distribution estimated from the Eureka ATM laser data.

There is potential that sea ice altimetry is subject to electromagnetic (EM) bias, where the mean height of specular sea ice facets, weighted by their backscattering contribution, is different to the mean height of the true snow-ice interface. This is a well-documented source of height bias in ocean altimetry [68]. Any EM height bias not accounted for in the waveform retracking step would result in sea ice freeboard or snow depth estimation uncertainty. Recently, [19] showed that roughness has a significant impact on ice thickness uncertainty and this may, in part, be due to roughness-induced electromagnetic bias. To verify this would require further airborne investigation with detailed *in situ* measurements at the locations of flat sea ice patches.

In this study, the effects of volume scattering could not be robustly investigated. However, 41% of the waveforms were discarded over FYI, and 51% over MYI, when estimating snow depths, based on our waveform filtering criteria. One of the criteria for filtering was that visible air-snow and snow-ice interfaces were well-separated without strong backscatter between and, in a portion of the discarded FYI waveforms, volume or internal interface scattering from snow may have obscured this separation. Including these discarded waveforms could increase the fraction of samples where incoherent radar scattering within the snowpack dominates the return power. However, these waveforms were discarded only during snow depth estimation, but were included in all other analyses of air-snow versus snow-ice interface backscattering.

## VII. CONCLUSIONS

This study aimed to understand which properties of snow and sea ice airborne Ku-band SAR altimetry is sensitive to and where the radar energy predominantly backscatters from. This study assessed the power and energy returns of the snow-ice and air-snow interfaces over Arctic sea ice, as functions of snow depth, roughness and across-track footprint slope, using airborne Ku-band altimetry in combination with ATM laser data. Over first year sea ice, the data supports that on the aircraft scale Ku-band radar backscattering from both the air-snow and snow-ice interfaces is primarily controlled by a probabilistic strong, quasi-specular scattering mechanism, with the specular component of the return being stronger for the snow-ice interface.

In many of the return waveforms that do not show a quasi-specular return from the snow-ice interface, the air-snow return power is comparable to the snow-ice interface return power and varies in relative magnitude. This means that without the fine range resolution of the OIB radar used in this study, empirical retracking thresholds would measure the height of the air-snow interface, the snow-ice interface, or the space between them, depending on the separation of waveform peaks footprint to footprint.

The relative contribution of coherent returns from, as well as the relative contributions of, the interfaces likely depends on the distance from which the sea ice is observed at. On the aircraft scales, the results of this paper suggest that the backscattered power/energy from the snow-ice interface is  $3 - 5 \times$  more dominant compared to the air-snow interface for FYI, though the backscattered power distribution of the snow-ice interface is highly positively skewed. Based on the coherence seen for the SIRAL returns at satellite scale for CryoSat-2, as well as the relationship between specular scattering and footprint slope observed at the aircraft scale, the majority of backscatter at Ku-band for high-altitude aircraft and satellite platforms is likely to originate from specular scattering as opposed to diffuse scattering. Most surface investigations have found that a significant portion of the Ku-band radar power is scattered from well above snow-ice interface; however, the bias that this would actually induce in satellite retrievals is not reflected by *in situ* validation with sensors like ULS buoys (e.g. [69]). Our results present an explanation for this apparent contradiction because the geometries and length-scales of the surface-based investigations do not necessarily reflect the situation for satellites.

There was only a minor (1.8 cm) underestimation of FYI snow depths, by the Ku-band radar, despite high basal salinity (5.0 ppt measured at the base 3 cm of the snowpack, and an average of 17.5 ppt at the snow-ice interface). This suggests that on the airborne scale, even if radar penetration through the snowpack is reduced by higher absorption from brine-wetted snow grains, the snow-ice interface can still be prominent if it produces a strong, quasi-specular reflection. The coherent return from the snow-ice interface is expected to be more pronounced for FYI than for MYI. Measurements of the ice freeboard and snow depth from radar altimeters could therefore generally become more accurate as the proportion of FYI



continues to increase within the Arctic basin [70].

This method represents an airborne proxy for the newly-aligned ICESat-2 and CryoSat-2 orbits of the Cryo2Ice campaign, and shows promise of accurate estimation of snow depths if the Ku-band air-snow interface peak can be accounted for or is less important at satellite altitudes. Further work is needed to characterise the proportionate power/energy returns from the air-snow and snow-ice interfaces and snow volume at satellite scales, and how snow properties affect these proportions. This demands *in situ* observations of the characteristic facet slope and height distributions of the air-snow and snow-ice interfaces, and whether facet slope and height distributions are correlated, across the relevant scales for satellite altimetry.

#### ACKNOWLEDGEMENTS

The authors would like to thank everyone who participated on the 2016 Snow on Sea Ice Campaign near Eureka led by Environment and Climate Change Canada (ECCC). This work is a contribution to The European Space Agency (ESA)'s "EXPRO+ Snow on Sea Ice" project under grant ESA AO/1-10061/19/I-EF. JL was supported by the INTERAAC project under grant #328957 from the Research Council of Norway and by the Fram Centre program for Sustainable Development of the Arctic Ocean (SUDARCO) under grant #2551323. RM acknowledges funding from the London NERC Doctoral Training Partnership (NE/L002485/1) and the Canada 150 Chair program via Professor Julianne Stroeve (G00321321). RW received funding from the European Union's Horizon 2020 research and innovation programme via project CRiceS (grant no. 101003826). The authors acknowledge the use of data and/or data products from CReSIS generated with support from the University of Kansas, NASA Operation Ice-Bridge grant NNX16AH54G, NSF grants ACI-1443054, OPP-1739003, and IIS-1838230, Lilly Endowment Incorporated, and Indiana METACyt Initiative.

#### APPENDICES

Appendix A contextualises the roughness and backscatter properties of the FYI site in relation to sea ice over the whole Arctic. Appendix B describes the altimetric calibration of the laser and radar data for this study in more detail. Appendix C shows an example echogram comparing the *in situ* measurements to the airborne estimates of the snow-ice interface. Finally, Appendix D describes how the distribution of measured slopes (on the 2 m scale) in a particular direction is compared to a distribution created by convolving two gaussian distributions: one defined by the error in measured slopes due to ATM height uncertainty (the uncertainty distribution), and the other representing the actual (errorless) slope distribution, which is adjusted so that the convolution of both the theoretical slope and error distribution matches the measured slope distribution.

#### APPENDIX A CONTEXTUALISING SITE ROUGHNESS

To contextualise how 'typical' the large-scale roughness of the Eureka site studied is of Arctic sea ice, the following comparisons have been made.

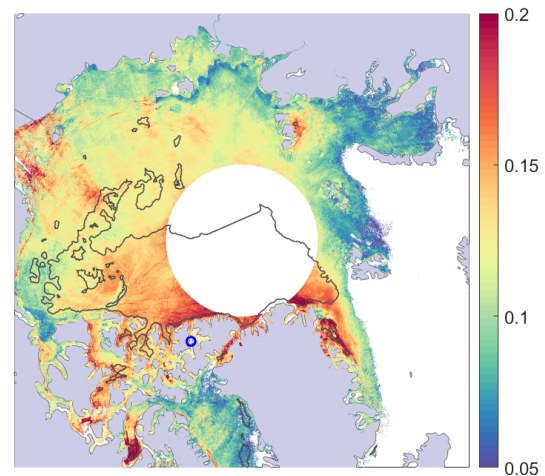


Fig. A1. Pan-Arctic April 2016 air-snow interface topography (height standard deviation) derived from the Multi-angle Imaging SpectroRadiometer (MISR) sensor at a resolution of 1 km by [46], with the contour separating mainly FYI versus mainly MYI from the OSI-SAF sea ice type product overlaid. The Eureka study site is highlighted by the blue circle.

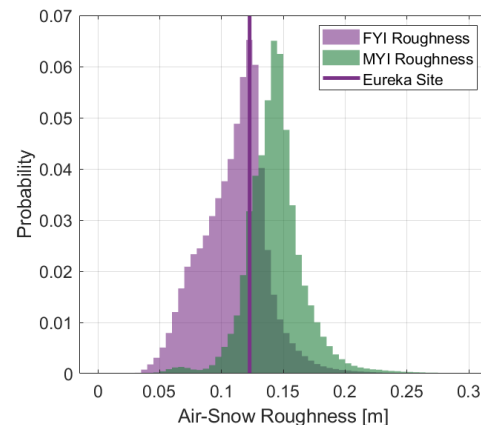


Fig. A2. Distributions of Pan-Arctic April 2016 air-snow interface topography for zones of FYI versus MYI, as defined by the OSI-SAF sea ice type product. The mean topography of sea ice within 2 km of the Eureka study site is shown by the purple line and coincides with the modal topography of pan-Arctic FYI.

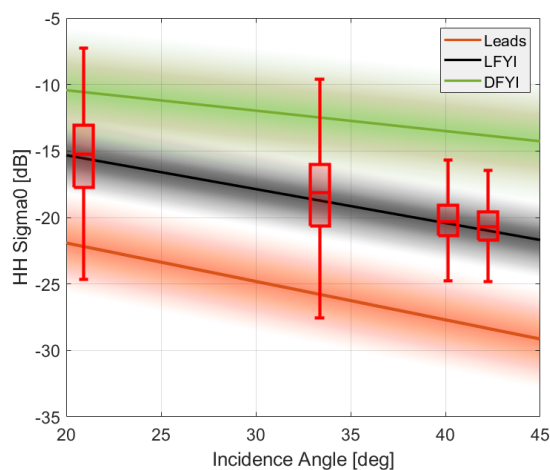


Fig. A3. Sentinel-1A C-band HH backscatter from the Eureka study site in April 2016 compared to the pan-Arctic manually generated ice type classification database of [45]. The boxplots show distributions of radar backscatter from four Sentinel-1A images in April 2016 with the Eureka study site located at different sensor incidence angles. The lines and shaded areas show the mean and standard deviation of ice type training polygons for leads, level first-year ice (LFYI) and deformed first-year ice (DFYI)

## APPENDIX B ALTIMETRIC ALIGNMENT

The offsets in height for the ATM laser data for each flyover, used to align all of the data to the same relative height, can be seen in Appendix B4. Once this offsetting is applied to the ATM laser data, the Ku-band SAR data of each flyover was altimetrically aligned to the ATM laser data by fixing heights of the 70% thresholds of the air-snow interface observed in some SAR waveforms to the mean ATM heights within corresponding footprints, shown in Appendix B5.

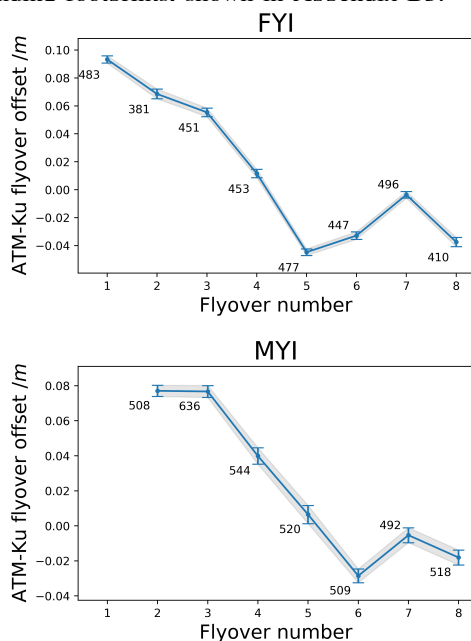


Fig. B5. The altimetric offsets between the mean of mean ATM laser altitudes within footprint and the mean altitude of the 70% thresholds of the air-snow interfaces seen in Ku-band SAR, for each flyover. The error bars correspond to the standard error of the differences between mean footprint ATM heights and retracked Ku-band SAR air-snow height.

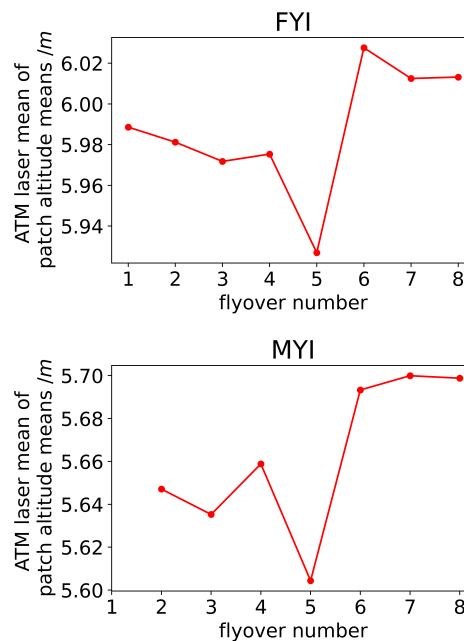


Fig. B4. Variations in effective mean ATM laser altitudes over Eureka firstyear ice (FYI) and multiyear ice (MYI) for different flyovers, relative to WGS84. These were used to align the ATM laser altitudes from each flyover to each other.

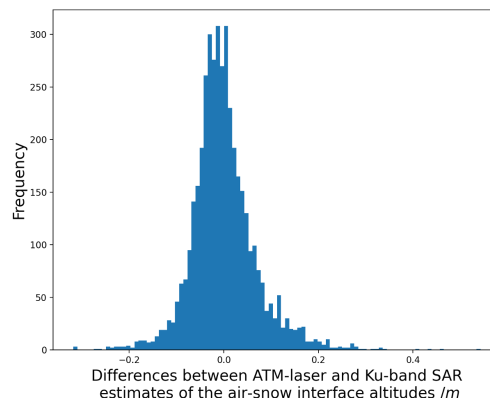


Fig. B6. Calibrated heights of the air-snow interface estimated by the SAR double-peaked echoes, subtracted from the air-snow heights estimated by the ATM laser data, over FYI.

## APPENDIX C EXAMPLE ECHOGRAM



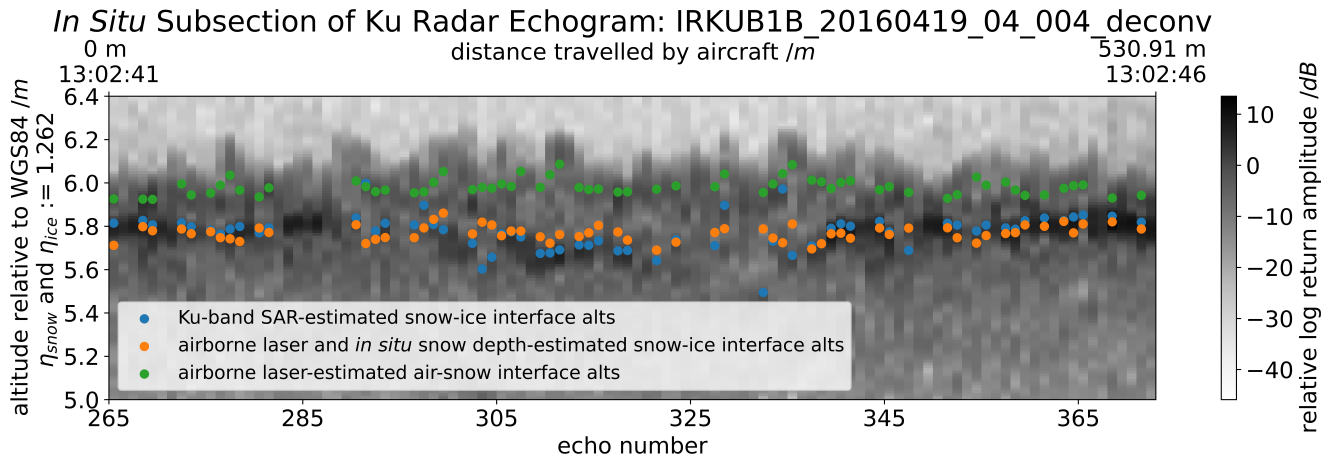


Fig. C7. Ku-band SAR echogram over the FYI *in situ* site. The estimates of the air-snow interface altitude is shown (in green) using the mean footprint ATM laser altitudes. Beyond these, the refractive indices of snow and ice have been set to 1.262. The estimates of the snow-ice interface using the airborne Ku-band SAR snow depth estimates subtracted from the ATM laser altitudes are shown in blue. The estimates of the snow-ice interface using the *in situ* snow depths subtracted from ATM laser altitudes are shown in orange. Scatter points are only shown for footprints where both airborne Ku-band SAR and *in situ* snow depth estimates exist.

## APPENDIX D

### ESTIMATING THE DISTRIBUTION OF FACET SLOPES

In order to estimate coherent returns from the ice, the facet slope distribution needed to be estimated. This was done by first observing the small-scale (using ATM laser data within a 2 m radius around different ATM laser points) slope distribution of the ATM laser data in a particular direction (1-D). In order to do this, at least four different ATM points surrounding a particular ATM point were required, with at least one in each horizontal quadrant, when projecting into the x-direction to calculate the slope gradient and its uncertainty. The data was collected from ATM laser files corresponding to the FYI Ku-band SAR files, and the files were not combined in case any errors in the ATM laser flyover offset corrections would affect the calculated slopes. Then the uncertainty in the slope distribution was accounted for by minimising the Kolmogorov-Smirnoff statistic when convolving the slope uncertainty distribution with a Gaussian distribution of varying standard deviation, so that the standard deviation of the Gaussian approximates the actual 1-D slope distribution (untainted by the uncertainty in ATM laser heights). The 2-D slope distribution was then approximated from the Pythagorean addition of 2 random 1-D slope distributions, assuming interface gradients in the x- and y- direction are independent, each with a standard deviation of 0.94 degrees. The comparison of the observed 1-D slope distribution to the convolution of the uncertainty distribution and the estimated actual 1-D slope distribution can be seen in Figure D8, and shows that the model fits the data well. The theoretical 2-D slope distribution is at the bottom of Figure D8. Note that the slope distribution estimated in this way from ATM laser data is assumed to roughly represent the slope distribution of the snow-ice interface.

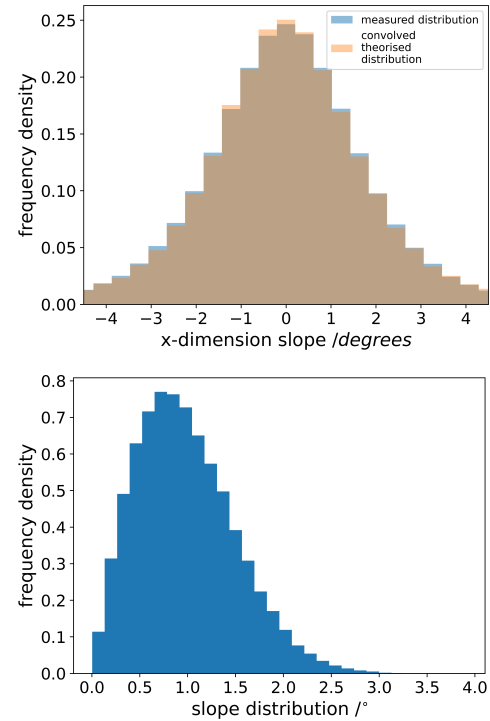


Fig. D8. Top: a comparison between the measured 1-D slope distribution, calculated using ATM laser data (in a 2 m radius), with a theoretical distribution generated by the convolution of a the slope uncertainty distribution and a 0-centered Gaussian representing the actual slope distribution (which has a standard deviation so that the theoretical convolved distribution generated closely matches the observed distribution). Bottom: resultant 2-D distribution of small-scale slopes predicted. This 2-D slope distribution is used to represent the facet slope distribution.

## REFERENCES

- [1] K. Giles, S. Laxon, D. Wingham, D. Wallis, W. Krabill, C. Leuschen, D. McAdoo, S. Manizade, and R. Raney, "Combined airborne laser and radar altimeter measurements over the fram strait in may 2002," *Remote Sensing of Environment*, vol. 111, no. 2-3, pp. 182–194, 2007.
- [2] R. Ricker, S. Hendricks, V. Helm, H. Skourup, and M. Davidson, "Sensitivity of cryosat-2 arctic sea-ice freeboard and thickness on radar-waveform interpretation," *Cryosphere*, vol. 8, no. 4, pp. 1607–1622, 2014.
- [3] R. L. Tilling, A. Ridout, and A. Shepherd, "Estimating arctic sea ice thickness and volume using cryosat-2 radar altimeter data," *Advances in Space Research*, vol. 62, no. 6, pp. 1203–1225, 2018.
- [4] R. D. Mallett, J. C. Stroeve, M. Tsamados, J. C. Landy, R. Willatt, V. Nandan, and G. E. Liston, "Faster decline and higher variability in the sea ice thickness of the marginal arctic seas when accounting for dynamic snow cover," *The Cryosphere*, vol. 15, no. 5, pp. 2429–2450, 2021.
- [5] I. A. Glissenaar, J. C. Landy, A. A. Petty, N. T. Kurtz, and J. C. Stroeve, "Impacts of snow data and processing methods on the interpretation of long-term changes in baffin bay early spring sea ice thickness," *The Cryosphere*, vol. 15, no. 10, pp. 4909–4927, 2021.
- [6] S. Laxon, N. Peacock, and D. Smith, "High interannual variability of sea ice thickness in the arctic region," *Nature*, vol. 425, no. 6961, pp. 947–950, 2003.
- [7] S. Hendricks, R. Ricker, and V. Helm, "Awi cryosat-2 sea ice thickness data product (v1. 2)," 2016.
- [8] F. Garnier, S. Fleury, G. Garric, J. Bouffard, M. Tsamados, A. Laforge, M. Bocquet, R. M. Fredensborg Hansen, and F. Remy, "Advances in altimetric snow depth estimates using bi-frequency saral and cryosat-2 ka-ku measurements," *The Cryosphere*, vol. 15, no. 12, pp. 5483–5512, 2021.
- [9] S. Beaven, G. Lockhart, S. Gogineni, A. Hosseini, K. Jezek, A. Gow, D. Perovich, A. Fung, and S. Tjuatja, "Laboratory measurements of radar backscatter from bare and snow-covered saline ice sheets," *Remote Sensing*, vol. 16, no. 5, pp. 851–876, 1995.
- [10] R. Kwok, H. J. Zwally, and D. Yi, "Icesat observations of arctic sea ice: A first look," *Geophysical Research Letters*, vol. 31, no. 16, 2004.
- [11] V. Nandan, R. Willatt, R. Mallett, J. Stroeve, T. Geldsetzer, R. Scharien, R. Tonboe, J. Landy, D. Clemens-Sewall, A. Jutila *et al.*, "Wind transport of snow impacts ka-and ku-band radar signatures on arctic sea ice," *The Cryosphere Discussions*, pp. 1–38, 2022.
- [12] R. C. Willatt, K. A. Giles, S. W. Laxon, L. Stone-Drake, and A. P. Worby, "Field investigations of ku-band radar penetration into snow cover on antarctic sea ice," *IEEE Transactions on Geoscience and remote sensing*, vol. 48, no. 1, pp. 365–372, 2010.
- [13] J. Stroeve, V. Nandan, R. Willatt, R. Tonboe, S. Hendricks, R. Ricker, J. Mead, R. Mallett, M. Huntemann, P. Itkin *et al.*, "Surface-based ku-and ka-band polarimetric radar for sea ice studies," *The Cryosphere*, vol. 14, no. 12, pp. 4405–4426, 2020.
- [14] K. A. Giles and S. M. Hvidegaard, "Comparison of space borne radar altimetry and airborne laser altimetry over sea ice in the fram strait," *International Journal of Remote Sensing*, vol. 27, no. 15, pp. 3105–3113, 2006.
- [15] R. Willatt, S. Laxon, K. Giles, R. Cullen, C. Haas, and V. Helm, "Ku-band radar penetration into snow cover on arctic sea ice using airborne data," *Annals of Glaciology*, vol. 52, no. 57, pp. 197–205, 2011.
- [16] R. Ricker, S. Hendricks, D. K. Perovich, V. Helm, and R. Gerdes, "Impact of snow accumulation on cryosat-2 range retrievals over arctic sea ice: An observational approach with buoy data," *Geophysical Research Letters*, vol. 42, no. 11, pp. 4447–4455, 2015.
- [17] V. Nandan, T. Geldsetzer, J. Yackel, M. Mahmud, R. Scharien, S. Howell, J. King, R. Ricker, and B. Else, "Effect of snow salinity on cryosat-2 arctic first-year sea ice freeboard measurements," *Geophysical Research Letters*, vol. 44, no. 20, pp. 10–419, 2017.
- [18] C. Nab, R. Mallett, W. Gregory, J. Landy, I. Lawrence, R. Willatt, J. Stroeve, and M. Tsamados, "Synoptic variability in satellite altimeter-derived radar freeboard of arctic sea ice," *Geophysical Research Letters*, p. e2022GL100696, 2023.
- [19] J. C. Landy, A. A. Petty, M. Tsamados, and J. C. Stroeve, "Sea ice roughness overlooked as a key source of uncertainty in cryosat-2 ice freeboard retrievals," *Journal of Geophysical Research: Oceans*, vol. 125, no. 5, p. e2019JC015820, 2020.
- [20] V. Helm, A. Humbert, and H. Miller, "Elevation and elevation change of greenland and antarctica derived from cryosat-2," *The Cryosphere*, vol. 8, no. 4, pp. 1539–1559, 2014.
- [21] J. King, H. Skourup, S. M. Hvidegaard, A. Rösel, S. Gerland, G. Spreen, C. Polashenski, V. Helm, and G. E. Liston, "Comparison of freeboard retrieval and ice thickness calculation from als, asiras, and cryosat-2 in the norwegian arctic to field measurements made during the n-ice2015 expedition," *Journal of Geophysical Research: Oceans*, vol. 123, no. 2, pp. 1123–1141, 2018.
- [22] M. Meloni, J. Bouffard, T. Parrinello, G. Dawson, F. Garnier, V. Helm, A. Di Bella, S. Hendricks, R. Ricker, E. Webb *et al.*, "Cryosat ice baseline-d validation and evolutions," *The Cryosphere*, vol. 14, no. 6, pp. 1889–1907, 2020.
- [23] J. Stroeve, V. Nandan, R. Willatt, R. Dadic, P. Rotosky, M. Gallagher, R. Mallett, A. Barrett, S. Hendricks, R. Tonboe *et al.*, "Rain-on-snow (ros) understudied in sea ice remote sensing: A multi-sensor analysis of ros during mosaic," *Cryosphere Discussions*, 2022.
- [24] N. T. Kurtz, N. Galin, and M. Studinger, "An improved cryosat-2 sea ice freeboard retrieval algorithm through the use of waveform fitting," *The Cryosphere*, vol. 8, no. 4, pp. 1217–1237, 2014.
- [25] H. J. Eom, *Theoretical scatter and emission models for microwave remote sensing*. University of Kansas, 1982.
- [26] A. Fung and H. Eom, "Coherent scattering of a spherical wave from an irregular surface," *IEEE Transactions on Antennas and Propagation*, vol. 31, no. 1, pp. 68–72, 1983.
- [27] A. Fung, W. Liu, K.-S. Chen, and M. Tsay, "An improved iem model for bistatic scattering from rough surfaces," *Journal of Electromagnetic Waves and Applications*, vol. 16, no. 5, pp. 689–702, 2002.
- [28] L. Tsang, J. Pan, D. Liang, Z. Li, D. W. Cline, and Y. Tan, "Modeling active microwave remote sensing of snow using dense media radiative transfer (dmrt) theory with multiple-scattering effects," *IEEE Transactions on Geoscience and Remote Sensing*, vol. 45, no. 4, pp. 990–1004, 2007.
- [29] W. Chang, S. Tan, J. Lemmetyinen, L. Tsang, X. Xu, and S. H. Yueh, "Dense media radiative transfer applied to snowscat and snowsar," *IEEE Journal of Selected Topics in Applied Earth Observations and Remote Sensing*, vol. 7, no. 9, pp. 3811–3825, 2014.
- [30] J. King, R. Kelly, A. Kasurak, C. Duguay, G. Gunn, N. Rutter, T. Watts, and C. Derksen, "Spatio-temporal influence of tundra snow properties on ku-band (17.2 ghz) backscatter," *Journal of Glaciology*, vol. 61, no. 226, pp. 267–279, 2015.
- [31] F. M. Fetterer, M. R. Drinkwater, K. C. Jezek, S. W. Laxon, R. G. Onstott, and L. M. Ulander, "Sea ice altimetry," in *Microwave Remote Sensing of Sea Ice*. 2000 Florida Avenue, NW, Washington, DC 20009: American Geophysical Union, 1992, pp. 117–119.
- [32] F. Ulaby, D. Long, W. Blackwell, C. Elachi, A. Fung, C. Ruf, K. Sarabandi, H. Zebker, and J. van Zyl, *Microwave radar and radiometric remote sensing*. The University of Michigan Press, 2015.
- [33] M. R. Drinkwater, "Ku band airborne radar altimeter observations of marginal sea ice during the 1984 marginal ice zone experiment," *Journal of Geophysical Research: Oceans*, vol. 96, no. C3, pp. 4555–4572, 1991.
- [34] P. Beckmann and A. Spizzichino, *The Scattering of Electromagnetic Waves from Rough Surfaces*. Pergamon Press, Oxford, 1963.
- [35] F. T. Ulaby, R. K. Moore, and A. K. Fung, *Microwave remote sensing: Active and passive. Volume 3-From theory to applications*. Artech House, 1986.
- [36] S. Laxon, "Sea ice altimeter processing scheme at the eodc," *International Journal of Remote Sensing*, vol. 15, no. 4, pp. 915–924, 1994.
- [37] C. Rapley, H. Griffiths, V. Squire, J. Oliver, A. Birks, A. Cooper, A. Cowan, D. Drewry, M. Gorman, M. Guzowska, S. Laxon, I. Mason, N. McIntyre, E. Novotny, R. Paterson, R. Scott, and F. Street-Perrot, *Applications and scientific uses of ERS-1 radar altimeter data (Final Report)*. European Space Agency, 02 1985.
- [38] J. Paden, J. Li, C. Leuschen, F. Rodriguez-Morales, and R. Hale, *IceBridge KuBand Radar LIB Geolocated Radar Echo Strength Profiles, Version 2, userguide 1*. NASA National Snow and Ice Data Center Distributed Active Archive Center, Boulder, Colorado USA, 2014, updated 2017, accessed: 2022-09-06.
- [39] M. Studinger, *IceBridge ATM LIB Elevation and Return Strength, Version 2, userguide 2*. NASA National Snow and Ice Data Center Distributed Active Archive Center, Boulder, Colorado USA, 2013, updated 2020, accessed: 2022-09-06.
- [40] D. Yi, J. P. Harbeck, S. S. Manizade, N. T. Kurtz, M. Studinger, and M. Hofton, "Arctic sea ice freeboard retrieval with waveform characteristics for nasa's airborne topographic mapper (atm) and land, vegetation, and ice sensor (lvis)," *IEEE Transactions on Geoscience and Remote Sensing*, vol. 53, no. 3, pp. 1403–1410, 2015.
- [41] K. M. Brunt, R. L. Hawley, E. R. Lutz, M. Studinger, J. G. Sonntag, M. A. Hofton, L. C. Andrews, and T. A. Neumann, "Assessment of nasa

- airborne laser altimetry data using ground-based gps data near summit station, greenland," *The Cryosphere*, vol. 11, no. 2, pp. 681–692, 2017.
- [42] J. King, S. Howell, M. Brady, P. Toose, C. Derksen, C. Haas, and J. Beckers, "Local-scale variability of snow density on arctic sea ice," *The Cryosphere*, vol. 14, no. 12, pp. 4323–4339, 2020.
- [43] "Daily data report for april 2016 - eureka a nunavut," [https://climate.weather.gc.ca/climate\\_data/daily\\_data\\_e.html?hlyRange=2016-02-22%7C2023-01-24&dlyRange=2016-02-25%7C2018-10-29&mlyRange=%7C&StationID=53598&Prov=NU&urlExtension=\\_e.html&searchType=stnProv&optLimit=yearRange&StartYear=2016&EndYear=2016&selRowPerPage=25&Line=37&lstProvince=NU&timeframe=2&time=LST&Year=2016&Month=4&Day=16](https://climate.weather.gc.ca/climate_data/daily_data_e.html?hlyRange=2016-02-22%7C2023-01-24&dlyRange=2016-02-25%7C2018-10-29&mlyRange=%7C&StationID=53598&Prov=NU&urlExtension=_e.html&searchType=stnProv&optLimit=yearRange&StartYear=2016&EndYear=2016&selRowPerPage=25&Line=37&lstProvince=NU&timeframe=2&time=LST&Year=2016&Month=4&Day=16), accessed: 2023-01-31.
- [44] M. Zygmuntowska and K. Khvorostovsky, "Analysis of cryosat's radar altimeter waveforms over different arctic sea ice regimes," *Arctic sea ice altimetry-advances and current uncertainties*, 2014.
- [45] J. Lohse, A. P. Douglis, and W. Dierking, "Mapping sea-ice types from sentinel-1 considering the surface-type dependent effect of incidence angle," *Annals of Glaciology*, vol. 61, no. 83, pp. 260–270, 2020.
- [46] T. Johnson, M. Tsamados, J.-P. Muller, and J. Stroeve, "Mapping arctic sea-ice surface roughness with multi-angle imaging spectroradiometer," *Remote Sensing*, vol. 14, no. 24, p. 6249, 2022.
- [47] R. Dominguez, *IceBridge DMS LIB Geolocated and Orthorectified Images, Version 1, userguide 1*. NASA National Snow and Ice Data Center Distributed Active Archive Center, Boulder, Colorado USA, 2010, updated 2018, accessed: 2022-09-06.
- [48] D. Wingham, C. Francis, S. Baker, C. Bouzinac, D. Brockley, R. Cullen, P. de Chateau-Thierry, S. Laxon, U. Mallow, C. Mavrocordatos *et al.*, "Cryosat: A mission to determine the fluctuations in earth's land and marine ice fields," *Advances in Space Research*, vol. 37, no. 4, pp. 841–871, 2006.
- [49] S. W. Laxon, K. A. Giles, A. L. Ridout, D. J. Wingham, R. Willatt, R. Cullen, R. Kwok, A. Schweiger, J. Zhang, C. Haas *et al.*, "Cryosat-2 estimates of arctic sea ice thickness and volume," *Geophysical Research Letters*, vol. 40, no. 4, pp. 732–737, 2013.
- [50] W. Xia and H. Xie, "Assessing three waveform retracers on sea ice freeboard retrieval from cryosat-2 using operation icebridge airborne altimetry datasets," *Remote Sensing of Environment*, vol. 204, pp. 456–471, 2018.
- [51] T. Newman, S. L. Farrell, J. Richter-Menge, L. N. Connor, N. T. Kurtz, B. C. Elder, and D. McAdoo, "Assessment of radar-derived snow depth over a rctic sea ice," *Journal of Geophysical Research: Oceans*, vol. 119, no. 12, pp. 8578–8602, 2014.
- [52] R. Kwok, "Simulated effects of a snow layer on retrieval of cryosat-2 sea ice freeboard," *Geophysical Research Letters*, vol. 41, no. 14, pp. 5014–5020, 2014.
- [53] V. Nandan, R. K. Scharien, T. Geldsetzer, R. Kwok, J. J. Yackel, M. S. Mahmud, A. Rösel, R. Tonboe, M. Granskog, R. Willatt *et al.*, "Snow property controls on modeled ku-band altimeter estimates of first-year sea ice thickness: Case studies from the canadian and norwegian arctic," *IEEE Journal of Selected Topics in Applied Earth Observations and Remote Sensing*, vol. 13, pp. 1082–1096, 2020.
- [54] M. A. Webster, M. Holland, N. C. Wright, S. Hendricks, N. Hutter, P. Itkin, B. Light, F. Linhardt, D. K. Perovich, I. A. Raphael *et al.*, "Spatiotemporal evolution of melt ponds on arctic sea ice: Mosaic observations and model results," *Elem Sci Anth*, vol. 10, no. 1, p. 000072, 2022.
- [55] A. A. Petty, M. C. Tsamados, and N. T. Kurtz, "Atmospheric form drag coefficients over arctic sea ice using remotely sensed ice topography data, spring 2009–2015," *Journal of Geophysical Research: Earth Surface*, vol. 122, no. 8, pp. 1472–1490, 2017.
- [56] R. M. Fredensborg Hansen, E. Rinne, and H. Skourup, "Classification of sea ice types in the arctic by radar echoes from saral/altika," *Remote Sensing*, vol. 13, no. 16, p. 3183, 2021.
- [57] F. Pedregosa, G. Varoquaux, A. Gramfort, V. Michel, B. Thirion, O. Grisel, M. Blondel, P. Prettenhofer, R. Weiss, V. Dubourg, J. Vanderplas, A. Passos, D. Cournapeau, M. Brucher, M. Perrot, and E. Duchesnay, "Scikit-learn: Machine learning in Python," *Journal of Machine Learning Research*, vol. 12, pp. 2825–2830, 2011.
- [58] C. Rapley, H. Griffiths, V. Squire, M. Lefebvre, A. Birks, A. Brenner, C. Brossier, L. Clifford, A. Cooper, and A. Cowan, *A study of satellite radar altimeter operation over ice-covered surfaces*. European Space Agency, 1983.
- [59] J. C. Landy, M. Tsamados, and R. K. Scharien, "A facet-based numerical model for simulating sar altimeter echoes from heterogeneous sea ice surfaces," *IEEE Transactions on Geoscience and Remote Sensing*, vol. 57, no. 7, pp. 4164–4180, 2019.
- [60] A. Manninen, "Surface roughness of baltic sea ice," *Journal of Geophysical Research: Oceans*, vol. 102, no. C1, pp. 1119–1139, 1997.
- [61] S. Hong and I. Shin, "Global trends of sea ice: Small-scale roughness and refractive index," *Journal of Climate*, vol. 23, no. 17, pp. 4669–4676, 2010.
- [62] J. C. Landy, D. Isleifson, A. S. Komarov, and D. G. Barber, "Parameterization of centimeter-scale sea ice surface roughness using terrestrial lidar," *IEEE transactions on geoscience and remote sensing*, vol. 53, no. 3, pp. 1271–1286, 2015.
- [63] M. R. Drinkwater and J. A. Dowdeswell, "A multi-sensor approach to the interpretation of radar altimeter wave forms from two arctic ice caps," *Annals of Glaciology*, vol. 9, pp. 60–68, 1987.
- [64] A. K. Fung and K.-S. Chen, "An update on the iem surface backscattering model," *IEEE Geoscience and Remote Sensing Letters*, vol. 1, no. 2, pp. 75–77, 2004.
- [65] A. K. Fung and K. Chen, *Microwave scattering and emission models for users*. Artech house, 2010.
- [66] S. Lee, J. Im, J. Kim, M. Kim, M. Shin, H.-c. Kim, and L. Quackenbush, "Arctic sea ice thickness estimation from cryosat-2 satellite data using machine learning-based lead detection," *Remote Sensing*, vol. 8, no. 9, p. 698, 2016.
- [67] S. Paul, S. Hendricks, R. Ricker, S. Kern, and E. Rinne, "Empirical parametrization of envisat freeboard retrieval of arctic and antarctic sea ice based on cryosat-2: progress in the esa climate change initiative," *The Cryosphere*, vol. 12, no. 7, pp. 2437–2460, 2018.
- [68] B. S. Yapple, A. Shapiro, D. L. Hammond, B. D. Au, and E. A. Uliana, "Nanosecond radar observations of the ocean surface from a stable platform," *IEEE Transactions on Geoscience Electronics*, vol. 9, no. 3, pp. 170–174, 1971.
- [69] J. C. Landy, G. J. Dawson, M. Tsamados, M. Bushuk, J. C. Stroeve, S. E. Howell, T. Krumpen, D. G. Babb, A. S. Komarov, H. D. Heorton *et al.*, "A year-round satellite sea-ice thickness record from cryosat-2," *Nature*, vol. 609, no. 7927, pp. 517–522, 2022.
- [70] M. A. Tschudi, W. N. Meier, and J. S. Stewart, "An enhancement to sea ice motion and age products at the national snow and ice data center (nsidc)," *The Cryosphere*, vol. 14, no. 5, pp. 1519–1536, 2020.